PCCP

Reactive Quenching of NO ($A^2\Sigma^+$) with H_2O Leads to HONO: A Theoretical Analysis of the Reactive and Nonreactive Electronic Quenching Mechanisms

Journal:	*Physical Chemistry Chemical Physics*
Manuscript ID	CP-ART-09-2022-004214.R1
Article Type:	Paper
Date Submitted by the Author:	18-Oct-2022
Complete List of Authors:	Guardado, Jose; California State University Fullerton, Chemistry and Biochemistry Urquilla, Justin; California State University Fullerton, Chemistry and Biochemistry Kidwell, Nathanael; College of William And Mary Department of Chemistry, Petit, Andrew; California State University Fullerton, Chemistry and Biochemistry

Reactive Quenching of NO ($A^2\Sigma^+$) with H_2O Leads to HONO: A Theoretical Analysis of the Reactive and Nonreactive Electronic Quenching Mechanisms

José L. Guardado,[1] Justin A. Urquilla,[1] Nathanael M. Kidwell,[2] Andrew S. Petit,*[1]

[1] *Department of Chemistry and Biochemistry, California State University – Fullerton, Fullerton, CA 92834-6866, USA*

[2] *Department of Chemistry, The College of William and Mary, Williamsburg, VA 23187-8795, USA*

* Author to whom correspondence should be addressed. E-mail: apetit@fullerton.edu

Abstract

The electronic quenching of NO ($A^2\Sigma^+$) with molecular partners exemplifies the rich non-adiabatic dynamics that occurs on multiple, coupled potential energy surfaces (PESs). The mechanistic details of the electronic quenching depend sensitively on the nature and strength of the intermolecular interactions between NO ($A^2\Sigma^+$) and the molecular partner. In this paper, we reveal the electronic quenching mechanisms of NO ($A^2\Sigma^+$) with H_2O, a non-adiabatic process with an extremely large cross section of 121 Å^2 near room temperature. In doing so, we demonstrate that the NO ($A^2\Sigma^+$)+H_2O PES funnels a wide range of initial intermolecular orientations to the same minimum-energy geometry. Furthermore, we reveal low-energy pathways to conical intersections between NO ($A^2\Sigma^+$)+H_2O and NO ($X^2\Pi$)+H_2O that primarily involve decreasing the intermolecular distance and elongating a single O-H bond of H_2O. Based on these geometric distortions, we predict that nonreactive electronic quenching will be associated with significant vibrational excitation in a local O-H stretch mode in H_2O. Reactive quenching will produce a H-atom and HONO, an important intermediate in atmospheric and combustion chemistry and a precursor to the hydroxyl radical. Overall, our work provides the first detailed theoretical study of the mechanism of the electronic quenching of NO ($A^2\Sigma^+$) with a polyatomic molecular partner, as well as makes concrete predictions to inform future velocity map imaging experiments.

Introduction

Laser-induced fluorescence (LIF) on the $A^2\Sigma^+ \leftarrow X^2\Pi$ transition band is a well-established tool used to quantify nitric oxide (NO) concentrations in the atmosphere and operating combustion engines.[1–4] However, molecules and atoms present in these environments interfere with the LIF quantification of NO through electronic quenching. In electronic quenching, collisions between NO ($A^2\Sigma^+$) and an atomic or molecular partner provide nonradiative pathways back to the electronic ground state that compete with fluorescence. In fact, depending on the collisional partner, electronic quenching can dominate over fluorescence.[5–7] Therefore, electronic quenching may strongly affect the measured LIF intensities, leading to an underestimate of the true NO concentration.

To correct for inaccuracies in the determination of NO concentrations from LIF measurements, electronic quenching cross sections of known collisional partners have been experimentally measured.[6–10] Settersten and co-workers reported experimentally determined electronic quenching cross sections of NO ($A^2\Sigma^+$) with different collisional partners at various temperatures. Table 1 shows that NO ($A^2\Sigma^+$)+H_2O has an electronic quenching cross section of 121 Å^2 at 294 K.[9] This is significantly larger than the electronic quenching cross sections of NO ($A^2\Sigma^+$) with N_2, CO, and O_2 at 294 K: 0.007 Å^2, 6.55 Å^2, and 28.5 Å^2, respectively.[10] Additionally, Table 1 shows that the electronic quenching cross section of the NO ($A^2\Sigma^+$)+N_2 system increases as the temperature is increased above 294 K, that is, $\left.\frac{d\sigma}{dT}\right|_{T=294\ K} > 0$. In contrast, $\left.\frac{d\sigma}{dT}\right|_{T=294\ K} < 0$ for the other molecular partners. This suggests that electronic quenching in these systems proceeds through a NO ($A^2\Sigma^+$)+M collision complex whose formation is more likely at lower temperatures.[9,10] While experimental electronic quenching cross sections are useful to correct the LIF measurements of NO ($A^2\Sigma^+$), the underlying photochemical mechanisms responsible for

electronic quenching are still not well understood.

Table 1. Experimentally determined electronic quenching cross sections of NO ($A^2\Sigma^+$) with the Molecular Partners N_2, CO, O_2, and H_2O.[9,10]

Molecular Partner	Electronic Quenching Cross Section (σ) at 294 K	Sign of $\frac{d\sigma}{dT}\Big\vert_{T = 294\ K}$
N_2	0.007 Å^2	>0
CO	6.55 Å^2	<0
O_2	28.5 Å^2	<0
H_2O	121 Å^2	<0

Using NO ($A^2\Sigma^+$)+H_2O as an example, collisions between NO ($A^2\Sigma^+$) and H_2O can result in three different classes of energy-exchange pathways:

$$\mathrm{NO}\left(A^2\Sigma^+, v_i, J_i\right) + \mathrm{H_2O}\left(X^1A_1, v_{i,2}, J_{i,2}\right) \rightarrow \mathrm{NO}\left(A^2\Sigma^+, v_f, J_f\right) + \mathrm{H_2O}\left(X^1A_1, v_{f,2}, J_{f,2}\right) \quad (1)$$

$$\mathrm{NO}\left(A^2\Sigma^+\right) + \mathrm{H_2O} \rightarrow \mathrm{NO}\left(X^2\Pi\right) + \mathrm{H_2O} \quad (2)$$

$$\mathrm{NO}\left(A^2\Sigma^+\right) + \mathrm{H_2O} \rightarrow \mathrm{HONO} + \mathrm{H} \quad (3)$$

The first channel represents an inelastic collision in which energy is exchanged among the rovibrational levels of NO ($A^2\Sigma^+$) and H_2O; NO remains in its $A^2\Sigma^+$ excited electronic state. The second channel is an example of nonreactive electronic quenching resulting in a nonradiative NO ($A^2\Sigma^+$) → NO ($X^2\Pi$) transition, with the released energy partitioned among the nuclear degrees of freedom of the two molecules and relative translation. Because the lowest energy excited electronic state of H_2O lies above NO ($A^2\Sigma^+$), collisions between NO ($A^2\Sigma^+$) and H_2O cannot electronically excite the H_2O molecule. Lastly, the third channel exhibits reactive electronic quenching, in which the electronic excitation induces a chemical reaction. Channels 2 and 3 occur via conical intersections that couple the excited and ground electronic states of the NO-H_2O quenching pair.

A number of previous studies have focused on determining the underlying photochemical mechanisms of the electronic quenching of NO ($A^2\Sigma^+$) with atomic and molecular partners. The majority of these have focused on the collision channels of NO ($A^2\Sigma^+$) with rare gas atoms.[11–15] Studies involving molecular partners have primarily focused on the inelastic scattering channel (Equation 1). For example, Luxford and co-workers studied inelastic collisions between NO ($A^2\Sigma^+$) and D_2.[13] Their work demonstrated that the NO ($A^2\Sigma^+$)+D_2 PES is similar to that of NO ($A^2\Sigma^+$)+He but rotational energy transfer between NO ($A^2\Sigma^+$) and D_2 produces more anisotropic NO fragments than what is observed in NO ($A^2\Sigma^+$)+He.[13] In a theoretical study on the same system, Pajón-Suárez and co-workers developed an interaction PES for NO ($A^2\Sigma^+$) + H_2 over intermolecular distances ranging from 5−10 Å and showed that it was comparable to the interaction PES of NO ($A^2\Sigma^+$) with rare gas atoms.[16] In another experimental study, Luxford and co-workers utilized crossed molecular beams to probe inelastic rotational energy transfer in collisions between NO ($A^2\Sigma^+$) and N_2.[17] Their study revealed insights into the stereodynamics of the rotational energy transfer, with a clear preference for a linear ON−N_2 complex on the ON ($A^2\Sigma^+$)−N_2 PES with the N-atom of NO pointing toward N_2. More recently, Parsons and co-workers used velocity map imaging (VMI) to characterize the translational kinetic energy and NO ($A^2\Sigma^+$) rotational state distributions associated with the photodissociation of the NO+N_2 complex.[18–20] Finally, Soulié and Paterson recently published a NO ($A^2\Sigma^+$)+O_2 ($X^3\Sigma_g^-$) van der Waals PES, which contains a collision complex in an O-N-O-O linear geometry with an intermolecular distance of 4.3 Å and a binding energy of 95 cm^{-1}.[21]

Three recent studies on NO ($A^2\Sigma^+$)+O_2 are among the few that directly probe the mechanism of nonreactive electronic quenching of NO ($A^2\Sigma^+$) with a molecular partner. In the first, Few and co-workers used time-resolved Fourier-transform infrared emission spectroscopy to

measure vibrationally excited NO ($X^2\Pi$, v''=2–22) produced through nonreactive electronic quenching.[22] They observed a bimodal distribution which implied the presence of two channels. The first channel involves the production of NO ($X^2\Pi$) generated with high v'', along with O_2 co-products made in its $X^3\Pi_g^-$ or $a^1\Delta_g$ electronic state. The authors speculated that NO ($X^2\Pi$) produced with low v'' are formed from a second channel, which involves either the generation of O_2 ($c^1\Sigma_u^-$) via a harpoon mechanism or the formation of O_2 ($X^3\Pi_g^-$) through an inefficient process. More recently, Blackshaw and co-workers used VMI to determine the quantum-state resolved dynamical mechanisms of NO ($A^2\Sigma^+$)+O_2 nonreactive electronic quenching to NO ($X^2\Pi$, v''=0) products.[23] In this study, the relatively low total kinetic energy release (TKER) to products suggests that a significant fraction of the available energy is partitioned into the electronic, vibrational, and rotational levels of O_2. Phase space theory simulations of the TKER distribution show good agreement with the experimental data when O_2 is taken to be formed in its O_2 ($c^1\Sigma_u^-$) excited electronic state. As such, the outcomes from this nonreactive electronic quenching channel are consistent with the majority of the available energy ultimately ending up driving the electronic excitation of O_2. A recent theoretical study by Soulié and Paterson used multireference methods, SA-CASSCF and XMS-CASPT2, to develop a mechanistic rationalization of these experimental observations.[24] They identified two electronic quenching pathways, with the first proceeding via a transient ion-pair created by electron transfer from NO ($A^2\Sigma^+$) to O_2 and the second requiring significant elongation of the O_2 bond length. Soulié and Paterson argued that the first pathway exhibits a stronger dependence on the intermolecular orientation than the second. Moreover, the first pathway is predicted to produce greater vibrational excitation in the products due to the large geometric changes caused by the transient electron transfer.

Turning to the reactive electronic quenching pathway, Umemoto and co-workers experimentally probed the production of H atoms from collisions of NO ($A^2\Sigma^+$) with H_2O, C_2H_2, and C_2H_4.[25] In their experiments, a pump pulse excited the NO $A^2\Sigma^+ \leftarrow X^2\Pi$ band while a probe pulse monitored the formation of H-atoms via excitation to the 2^2S state. The electronically excited H atoms then underwent collisional relaxation to the 2^2P state which ultimately fluoresces in the vacuum ultraviolet, allowing for their detection. Analysis of the Doppler profile of the H-atom $2^2P \rightarrow 1^2S$ fluorescence signal suggested that a large fraction of the available energy, approximately 47.5% for NO ($A^2\Sigma^+$) + H_2O, is partitioned into translational kinetic energy. These observations suggested that the reactive electronic quenching process involves a short-lived collision complex. The authors speculated, as in Equation 3, that the reactive electronic quenching of NO ($A^2\Sigma^+$) with H_2O results in HONO formation. HONO plays a crucial atmospheric role in air quality, making the photochemistry of NO ($A^2\Sigma^+$) + H_2O of potential importance in atmospheric chemistry.[26] Umemeto and co-workers additionally reported CASSCF calculations performed on the NO+H_2O system in the C_s point group, which indicated that the lowest $^2A'$ state, which we will denote as D_1, adiabatically correlates to both the NO ($X^2\Pi$)+H_2O (X^1A_1) and H (^2S)+HONO ($^1A'$) product channels. This provides further support for HONO formation in the reactive electronic quenching process.

Outside of electronic quenching, several experimental and computational studies have focused on the NO+H_2O system. Lacome and co-workers performed experimental IR spectroscopy studies of NO+H_2O, NO+HDO, and NO+D_2O in a solid neon matrix.[27] Analysis of these spectra, along with electronic structure calculations performed at the B3LYP/6-311++G(2d,2p) level of theory, indicated that the most stable NO+H_2O complex geometry involves the nitrogen atom of NO hydrogen-bonding with H_2O. Salmi and co-workers obtained optimized geometries for

$NO+H_2O$ in both its $^2A'$ and $^2A''$ states (D_0 and D_1) at the CCSD(T)/A′VQZ level of theory.[28] They identified two $^2A'$ hydrogen-bonding conformers as well as two $^2A''$ electron donor-accepter complexes in which the oxygen atom of H_2O interacts with the nitrogen atom of NO; all four of these conformers are within 0.13 kcal/mol of each other. Additionally, Salmi and co-workers modeled the O-H stretching and H-O-H bending regions of the vibrational spectra of the $NO+H_2O$ conformers as well as the N-O stretching vibronic transitions of the $A^2\Sigma^+ \leftarrow X^2\Pi$ band. Finally, several additional theoretical studies have attempted to develop insights into the physical origin of the intermolecular interactions in the $NO+H_2O$ complex, as well as map out the D_0 and D_1 PESs.[29–31] Outside of the CASSCF calculations reported by Umemoto and co-workers, the photochemistry of NO ($A^2\Sigma^+$)+H_2O has not yet been explored.

Given the dearth of knowledge about the photochemical mechanisms responsible for NO ($A^2\Sigma^+$) electronic quenching with molecular partners, we recently performed a detailed theoretical study of the NO + H_2, NO + N_2, and NO + CO systems.[32] Figure 1 shows PESs calculated at the EOM-EA-CCSD/d-aug-cc-pVTZ//EOM-EA-CCSD/aug-cc-pVDZ level of theory for the D_2 (NO ($A^2\Sigma^+$)+M) and D_1 (NO ($X^2\Pi$)+M) states, where M is the collision partner, as a function of the intermolecular distance. The states are identified based on their electronic character at the asymptotic limit when NO+M are 10 Å apart. For each complex, the intermolecular orientation was constrained to a value that we previously identified to be most favorable for electronic quenching: $\theta_{CNO} = 120°$ for ON+CO, $\theta_{NNO} = 111°$ for ON+N_2, and $\theta_{HNO} = 111°$ for ON+H_2.

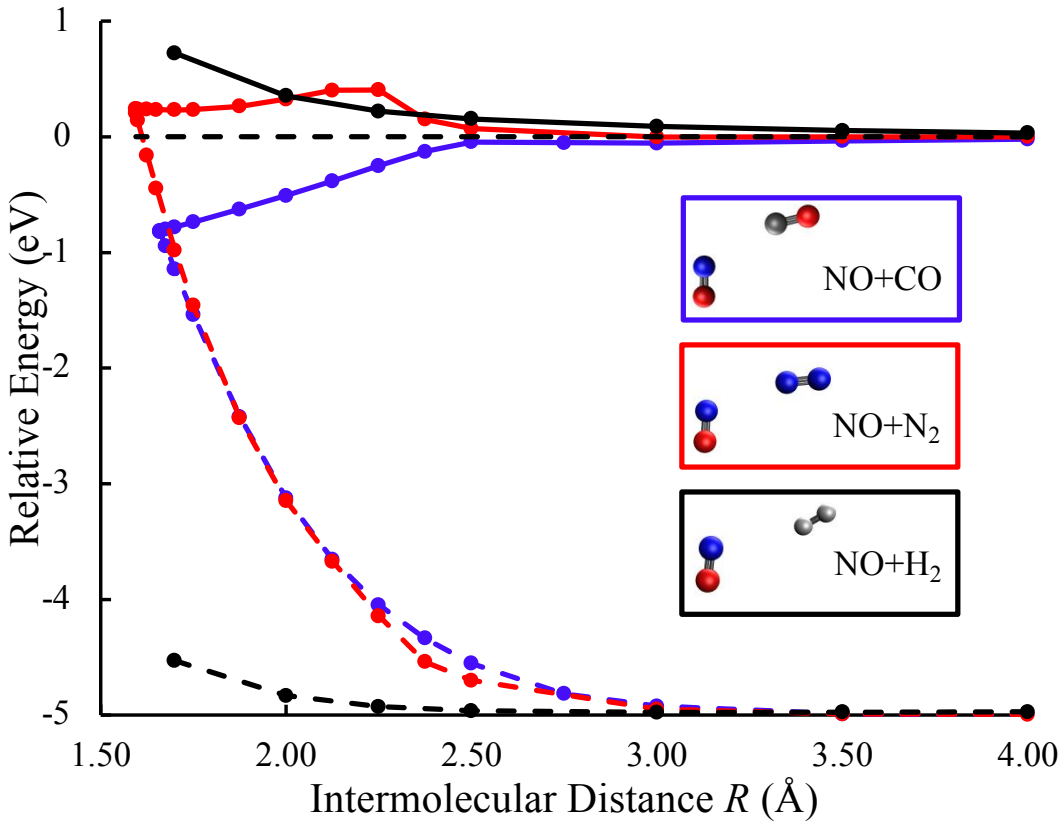

Figure 1. Cuts of the adiabatic PESs for the D_1 (dashed lines) and D_2 (solid lines) electronic states of the complexes ON+CO (blue lines), ON + N_2 (red lines), and ON + H_2 (black lines) along the intermolecular distance. All electronic energies are reported relative to NO ($A^2\Sigma^+$) + M at R=10 Å. Only the NO ($A^2\Sigma^+$) + CO system exhibits a downhill pathway to a D_2-D_1 conical intersection, which facilitates electronic quenching at low thermal energies. For further details, see our previous paper.[32]

The cuts of the PESs shown in Figure 1 reveal clear differences between the three systems, which reflect their experimental electronic quenching cross sections, as well as make predictions for future velocity map imaging (VMI) studies. While the D_1 PES is repulsive for all three systems, the D_2 PES is very different for each molecular partner. In particular, H_2 was the only molecular partner that showed no evidence of a conical intersection between D_2 and D_1 that would facilitate electronic quenching because both PESs are purely repulsive. Rather, it was predicted that inelastic scattering would be the primary deactivation mechanism for NO ($A^2\Sigma^+$) collisions with H_2. Although a D_2-D_1 conical intersection is formed for NO+N_2, it can only be reached if the colliding

molecules overcome a barrier of 0.404 eV. This suggests that there is a low probability for electronic quenching at low temperatures because the barrier will cause the internal conversion kinetics to be slower than the fluorescence rate of NO ($A^2\Sigma^+$); the approximate radiative lifetime of NO ($A^2\Sigma^+$) is 193 ns.[23] We posit that the NO ($A^2\Sigma^+$) + N_2 electronic quenching cross section increases from 0.007 Å^2 at 294 K to 0.116 Å^2 at 765 K due to the colliding molecules having greater thermal energy to surmount the barrier.[9] In contrast, NO ($A^2\Sigma^+$) has a higher electronic quenching cross section with CO because the D_2 PES has no barrier preceding the D_2-D_1 conical intersection. Moreover, this conical intersection lies below the asymptotic limit where the intermolecular interactions are attractive. Our data, therefore, explains why CO facilitates significantly greater electronic quenching of NO ($A^2\Sigma^+$) near room temperature than H_2 or N_2, which is reflected by the experimental cross section of 6.55 Å^2 at 294 K.

Figure 2 provides a more detailed description of the ON + CO PESs, with the six lowest-energy electronic states shown as a function of the intermolecular distance, R_{CN}, and a fixed intermolecular orientation of θ_{CNO} = 120°. The D_2 PES exhibits weak long-range attraction. Close to R_{CN}=2.50 Å, we see a drastic increase in the strength of the attractive intermolecular interactions on D_2 that funnels the colliding molecules into a D_2-D_1 conical intersection that lies well below the asymptotic limit. Further investigations led us to determine that the NO+CO PESs are significantly anisotropic, with only a narrow range of intermolecular orientations consistent with a downhill pathway to a D_2-D_1 conical intersection. Moreover, the D_2 PES is only very weakly attractive at intermolecular distances greater than 2.75 Å and is hence only able to guide the colliding molecules into the orientations that can reach the D_2-D_1 conical intersections when their translational and rotational energies are low. This is consistent with the experimental observation

that the NO ($A^2\Sigma^+$) + CO electronic quenching cross section increases from 6.55 Å^2 at 294 K to 13.6 Å^2 at 125 K.[9,10]

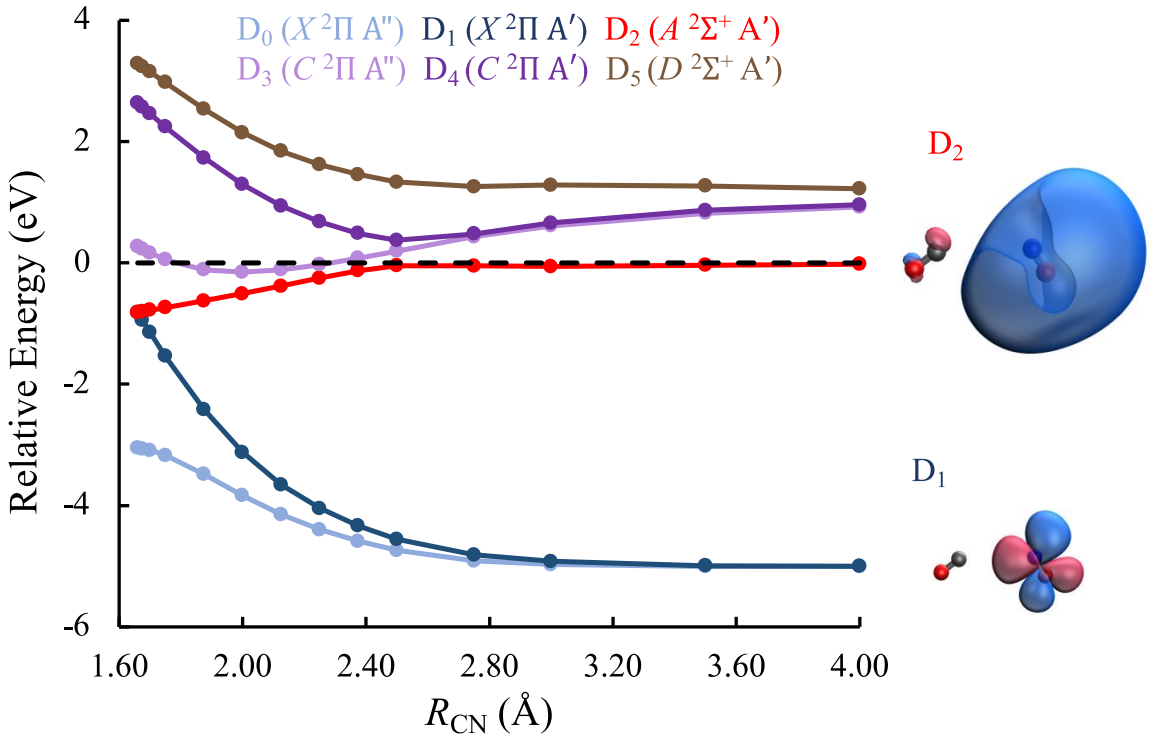

Figure 2. Cuts of the adiabatic PESs of the first six electronic states for ON + CO as a function of the distance between N and C (R_{CN}) at a fixed C−N−O angle (θ_{CNO}) of 120°; the remaining geometric parameters were optimized on D_2. The states are labeled based on their electronic character at R_{CN} = 10.0 Å, and all energies are reported relative to that of D_2 at R_{CN} = 10.0 Å. Around R_{CN}=2.50 Å, the strength of the intermolecular attractions on D_2 significantly increases, and the D_2 PES funnels population to the D_2-D_1 conical intersection. Additionally, note the apparent avoided crossing between D_2 and D_4 near R_{CN}=2.50 Å. For further details, see our previous paper.[32]

Figure 2 demonstrates that the electronic quenching of NO ($A^2\Sigma^+$) + CO is facilitated by the dramatic increase in intermolecular attractions below R_{CN}=2.50 Å. We attributed this to a harpoon mechanism, in which electron density shifts from the NO ($A^2\Sigma^+$) Rydberg orbital to the CO π* antibonding orbital, creating a transient ion pair that experiences Coulombic attractions.[8,32–35] The evidence for this is summarized in Figure 3. Panel 3A shows that as the two molecules move closer together, the electron spin density shifts from being localized on NO to being primarily

localized on CO. Similarly, panel 3B shows the development of significant partial positive charge on NO and partial negative charge on CO as R_{CN} is reduced. Importantly, the most significant redistribution of charge and spin density occurs between R_{CN} = 2.75 Å and R_{CN} = 2.50 Å, which is also the region where the D_2 PES becomes significantly attractive. The singly occupied molecular orbitals (SOMOs) shown in panel 3C provide additional support for a harpoon mechanism. At R_{CN} = 4 Å the SOMO is mostly localized on NO and displays clear 3sσ Rydberg character. As the intermolecular distance decreases, the SOMO develops greater amplitude on CO, eventually resembling the 2pπ* MO of CO with 3pπ Rydberg character on NO. This change in the electronic character of the D_2 state causes the development of bonding interactions between the two molecules and hence increased intermolecular attraction. In Figure 2, D_2 and D_4 appear to undergo an avoided crossing below 2.75 Å. In that vicinity, the SOMOs show an exchange in electronic character between D_2 and D_4. As D_2 begins to express 3pπ Rydberg character, D_4 takes on 3sσ Rydberg character.

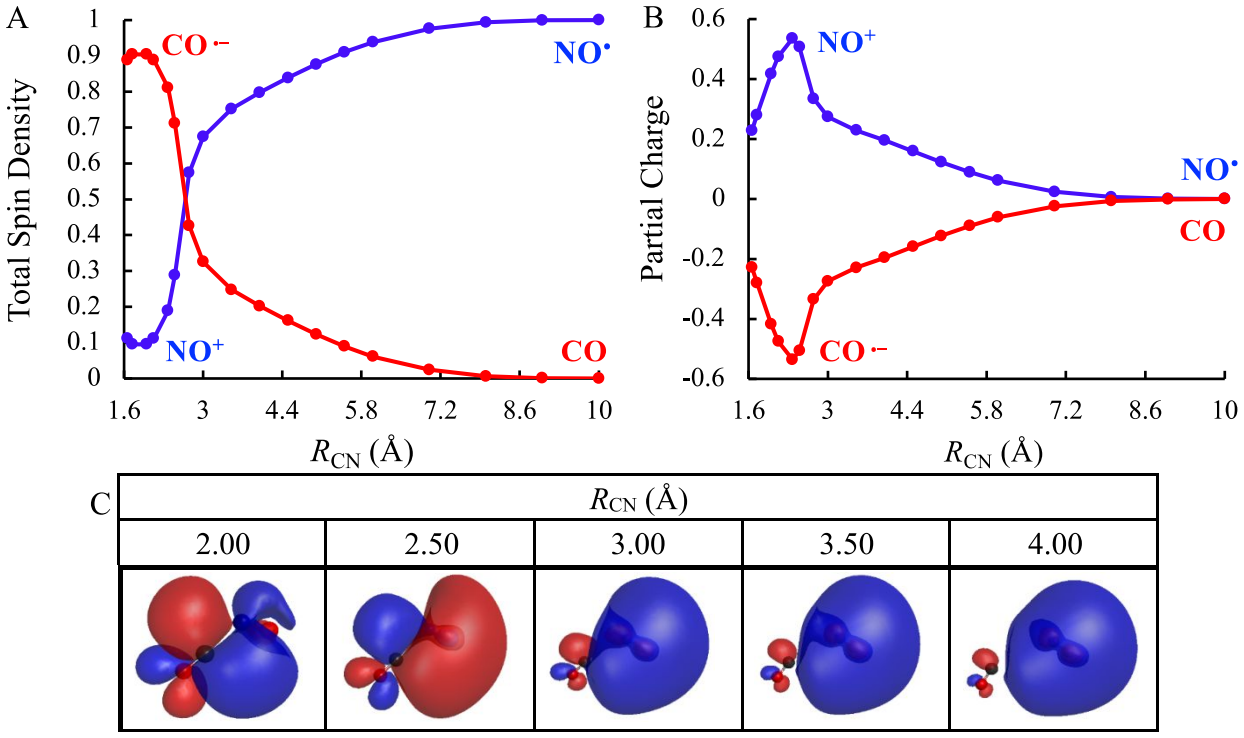

Figure 3. Löwdin population analysis for the total spin densities (panel A) and partial charges (panel B) of NO and CO as a function of the distance between N and C (R_{CN}) beginning at a fixed C−N−O angle (θ_{CNO}) of 120°. Panel C shows the SOMOs of D_2 at representative intermolecular distances. This analysis demonstrates that the increased intermolecular attraction between NO ($A^2\Sigma^+$) and CO on the D_2 PES, which occurs near R_{CN}=2.5 Å, is driven by electron transfer from NO to CO, i.e., a harpoon mechanism. For further details, see our previous paper.[32]

In the present study, we apply the theoretical analysis exemplified in Figures 1-3 to the NO+H_2O system. In doing so, we develop a mechanistic analysis for the 20-fold greater electronic quenching cross section of NO ($A^2\Sigma^+$) with H_2O compared with CO at 294 K. Through our analysis, we identify clear pathways for both nonreactive and reactive electronic quenching. We additionally demonstrate that a harpoon mechanism is responsible for the long-range intermolecular attractions that steer the colliding NO ($A^2\Sigma^+$) and H_2O molecules into a region of the D_2 PES that facilitates quenching. Throughout, we make clear predictions about the outcomes of NO ($A^2\Sigma^+$)+H_2O electronic quenching that will inform future velocity map imaging experiments. In particular, we demonstrate that the nonreactive electronic quenching pathway

results in the formation of HONO, an important intermediate in atmospheric chemistry that serves as a major source of hydroxyl radicals, OH.

Methods

The equation-of-motion electron attachment coupled-cluster singles and doubles (EOM-EA-CCSD) method in conjunction with an aug-cc-pVDZ basis was used to perform the initial geometry optimizations; mechanistically important pathways were re-optimized using the EOM-EA-CCSD/aug-cc-pVTZ level of theory. EOM-EA-CCSD utilizes the closed-shell NO^++H_2O reference to avoid the electronic structure challenges of using an open-shell NO+H_2O reference. This method accurately describes all target doublet states whose dominant electronic configurations can be built by adding an electron to a virtual orbital of the NO^++H_2O reference. This is true regardless of whether the states are characterized as valence or Rydberg orbitals, as well as whether or not the states have significant charge-transfer character.[36–38] The target states receive dynamic electron correlation through the inclusion of electron configurations that are doubly excited relative to the NO^++H_2O reference. Single-point calculations were performed at the EOM-EA-CCSD/d-aug-cc-pVTZ level of theory. We specifically chose a doubly augmented basis set to provide a reliable description of the Rydberg excited states of interest. All calculated energies are reported relative to the optimized NO ($A^2\Sigma^+$) + H_2O complex constrained to have an intermolecular distance of 10 Å. Our chosen computational approach was carefully benchmarked and justified in our previous paper.[32] In addition, in Figures S1-S3, we demonstrate that our approach provides the same overall mechanistic picture as the multireference method N-electron valence state perturbation theory (NVEPT2).[39,40] Unless otherwise stated, all calculations were performed using Q-Chem 5.4 and analyzed using IQmol 2.15.[41]

The EOM-EA-CCSD approach is known to be much less accurate for states with significant double excitation character.[36,37] We verified that all of the states analyzed in this study

consistently have dominant single excitation character. Indeed, doubly excited determinants always contributed less than 10% to the electronic wave function for all the states. In particular, we verified that all states of interest retain dominant single excitation character throughout the reactive electronic quenching pathways, which, as discussed below, involve stretching an O-H bond of water.

To investigate the electronic properties of the excited states, we used natural transition orbitals (NTOs) that were visualized with wxMacMolPlt.[42,43] Löwdin spin densities and partial charges were also investigated for all target states. To calculate both the NTOs and the Löwdin populations, we used the EOM-EA-CCSD/aug-cc-pVTZ level of theory.

Results and Discussion

Before mapping out cuts of the NO + H_2O PESs, we sought to identify the low-energy NO ($A^2\Sigma^+$) + H_2O collision complexes as well as to determine the degree of anisotropy in the asymptotic D_2 PES. We accomplished this by performing 272 unconstrained geometry optimizations that began in a wide variety of initial intermolecular orientations. We specifically explored NO-H_2O conformations in which the N or O atom of NO was oriented towards different sites of H_2O. For each overall arrangement, we varied the intermolecular orientation as well as sampled both planar and nonplanar geometries. For each starting geometry, the intermolecular distance was 3.50 Å.

The vast majority of the unconstrained geometry optimizations (242 out of 272) ultimately resulted in the same nonplanar collision complex with an intermolecular distance of R_{ON} = 1.91 Å and an energy of -0.57 eV relative to an optimized geometry on D_2 with R_{ON} = 10 Å. This nonplanar minimum-energy geometry is characterized by the NO lying above H_2O, the nitrogen of NO interacting with the oxygen of H_2O, and a H-O-N-O torsion angle of -178.6°; this ON-OH_2

collision complex is shown in the inset of Figure 4. Harmonic vibrational frequency analysis confirmed that this nonplanar geometry is a true minimum on the D_2 PES. While the majority of the 242 initial intermolecular orientations relaxed directly into the nonplanar collision complex, some led to low-energy saddle points with relative energies of -0.21 eV to -0.51 eV; all of these saddle points relaxed to the nonplanar collision complex after distorting along the imaginary frequency mode. These low-energy saddle points are primarily planar complexes or torsional conformers of the nonplanar collision complex.

The remaining 30 geometry optimizations can be classified into two groups. The first group, consisting of 23 geometry optimizations, relaxed into relatively high-energy saddle points with relative energies of -0.01 eV to 0.05 eV. Despite having high energies and significantly different geometries, all but one of these saddle points ultimately relaxed into the nonplanar collision complex discussed above after a geometric distortion along the imaginary frequency mode. The remaining 7 unconstrained geometry optimizations led to a nonplanar geometry where the oxygen of NO is directed towards the oxygen of H_2O with an intermolecular distance R_{OO} = 2.34 Å and a relative energy of -0.27 eV. Harmonic vibrational frequency analysis confirmed that this is a minimum on the D_2 PES. Analysis using the freezing string method and subsequent transition state geometry optimizations suggest that this local minimum re-arranges into the nonplanar ON-OH_2 collision complex with essentially no barrier.[44]

Collectively, our analysis suggests that the NO ($A^2\Sigma^+$)+H_2O PES is effective at funneling a large variety of initial intermolecular orientations into the same minimum energy geometry. This is in sharp contrast to what we previously observed with NO ($A^2\Sigma^+$) and CO, where the D_2 PES is much more anisotropic and only a narrow range of initial intermolecular orientations facilitate electronic quenching. As will be discussed below, the propensity for a large fraction of collisions

between NO ($A^2\Sigma^+$) and H_2O to relax into the low-energy collision complex on the D_2 PES helps to explain why the electronic quenching cross section of NO ($A^2\Sigma^+$)+H_2O is so large.

Figure 4 shows the cuts of the adiabatic PESs for the lowest six electronic states of NO with H_2O as a function of the intermolecular distance between NO and H_2O, R_{ON}, obtained by performing constrained geometry optimizations on D_2. We used the nonplanar collision complex with R_{ON} = 1.91 Å as the starting point for these adiabatic PESs. The two lowest energy states are labeled as D_0 ($X^2\Pi$) and D_1 ($X^2\Pi$), representing the half-filled π* orbital of the NO doublet radical parallel with or perpendicular to the plane of H_2O. These two states show degeneracy at large R_{ON} but have different energies at closer intermolecular distances due to the intermolecular interactions between NO and H_2O. At large intermolecular distances, the D_2 ($A^2\Sigma^+$) state is the 3sσ Rydberg state of NO mainly built from the 3s atomic orbitals. D_3 ($C^2\Pi$) and D_4 ($C^2\Pi$) are 3pπ Rydberg states and D_5 ($D^2\Sigma^+$) is a 3pσ Rydberg state; all of these states predominately consist of the unpaired electron residing in the 3p atomic orbitals of NO. The energies are reported relative to the D_2 energy at the D_2 optimized geometry of NO and H_2O constrained at R_{ON} = 10.0 Å.

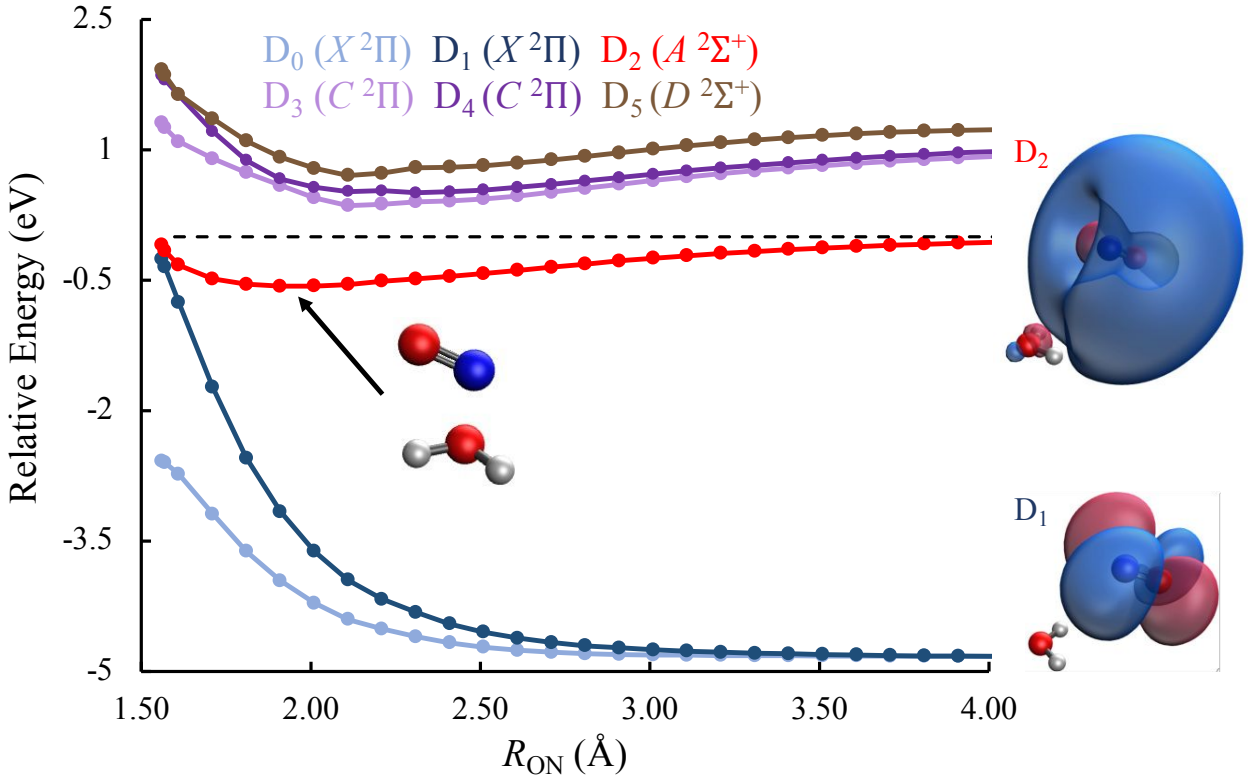

Figure 4. Cuts of the adiabatic PESs of the first six electronic states for NO+H_2O as a function of the distance between the N of NO and the O of H_2O, R_{ON}. All energies are reported relative to the D_2 state at R_{ON} = 10 Å. Note that long-range intermolecular attractions on D_2 lead to a collision complex (shown in the inset) with a relative energy of -0.57 eV. Unlike Figure 2, no low-energy D_2-D_1 conical intersection is present. The SOMOs associated with the D_1 and D_2 states are shown to the right of the PESs; these were evaluated at R_{ON} = 4.01 Å with an isovalue of 0.04.

As shown in Figure 4, the D_2 PES decreases in energy as the two molecules move closer together, signifying increased attractive intermolecular interactions. Eventually, the D_2 PES reaches a minimum at R_{ON} = 1.91 Å, where the energy of D_2 is -0.57 eV, well below the asymptotic limit. At intermolecular distances below 1.91 Å, the D_2 PES increases in energy as R_{ON} decreases, exceeding the asymptotic limit when R_{ON} < 1.55 Å. The D_0 and D_1 PESs are purely repulsive for all the intermolecular distances considered in Figure 4, with D_1 increasing faster as R_{ON} is reduced than D_0. The smallest energy gap between the D_2 and D_1 states identified in Figure 4 is 0.16 eV which occurs at R_{ON} = 1.55 Å and a D_2 relative energy of -0.02 eV. The higher-lying Rydberg

excited states, D_3-D_6, remain well-separated energetically from D_2 at all intermolecular distances that we examined in Figure 4.

The cuts of the NO+H_2O PESs shown in Figure 4 exhibit important similarities and differences from those of NO + CO shown in Figure 2. The D_2 PESs of both systems exhibit long-range attractions that facilitate electronic quenching. However, the magnitude of these intermolecular attractions is larger for NO ($A^2\Sigma^+$) + H_2O than for NO ($A^2\Sigma^+$) + CO. For example, the relative energy at a 3.0 Å intermolecular distance is -0.23 eV for NO ($A^2\Sigma^+$) + H_2O but only -0.06 eV for NO ($A^2\Sigma^+$) + CO. Moreover, while a large variety of initial intermolecular orientations of NO ($A^2\Sigma^+$) + H_2O are funneled to the same minimum-energy geometry, the PES cuts shown in Figure 2 are representative of a very limited range of initial intermolecular orientations of NO ($A^2\Sigma^+$) + CO; the majority of initial intermolecular orientations of NO ($A^2\Sigma^+$) + CO are not associated with a downhill pathway to a D_2-D_1 conical intersection. The stronger and less orientationally-dependent intermolecular attractions of NO ($A^2\Sigma^+$) + H_2O relative to NO ($A^2\Sigma^+$) + CO helps to explain the much larger electronic quenching cross section of H_2O. Figure 2 shows the presence of a D_2-D_1 conical intersection at an energy well below the asymptotic limit for the NO + CO system. No such low-energy D_2-D_1 conical intersection is present in Figure 4 for NO + H_2O. Since the experimental electronic quenching cross section of NO ($A^2\Sigma^+$) with H_2O is 20 times higher than with CO, a low-energy D_2-D_1 conical intersection must exist for NO + H_2O. Therefore, Figure 4 suggests that the pathway to the D_2-D_1 conical intersection responsible for electronic quenching involves a second nuclear degree of freedom beyond decreasing the intermolecular distance. Finally, we note that while Figure 2 shows an avoided crossing between the D_2 and D_4 states of NO + CO at R_{CN} = 2.50 Å, Figure 4 shows that no such avoided crossing occurs for the NO and H_2O system.

Before identifying a feasible pathway to a D_2-D_1 conical intersection, we first applied the analysis shown in Figure 3 to NO ($A^2\Sigma^+$) + H_2O to determine if a harpoon mechanism is responsible for the intermolecular attractions on the D_2 PES. Figure 5A shows the total spin densities of the NO and H_2O molecules, acquired by summing the Löwdin atomic spin densities in each molecule, as a function of the intermolecular distance, R_{ON}. Similarly, Figure 5B shows the total partial charges of the NO and H_2O molecules. In both panels, the NO data is shown in blue while the H_2O data is represented in red. For $R_{ON} \leq 4.75$ Å, the spin densities and partial charges were evaluated at the same geometries as were used in Figure 4. However, for 4.75 Å < R_{ON} < 10.00 Å, the Löwdin population analysis was performed on geometries obtained by rigidly increasing R_{ON} from the optimized geometry with R_{ON}=4.75 Å. No geometry optimizations were performed for these R_{ON} to bypass the orientational rearrangements that occurred in our constrained geometry optimizations when $R_{ON} > 4.75$ Å; such orientational rearrangements led to misleading plots by making R_{ON} no longer the smallest intermolecular distance. The inflection present in both panels of Figure 5 around R_{ON}=4.75 Å is a byproduct of this change in the procedure used to generate the molecular geometries.

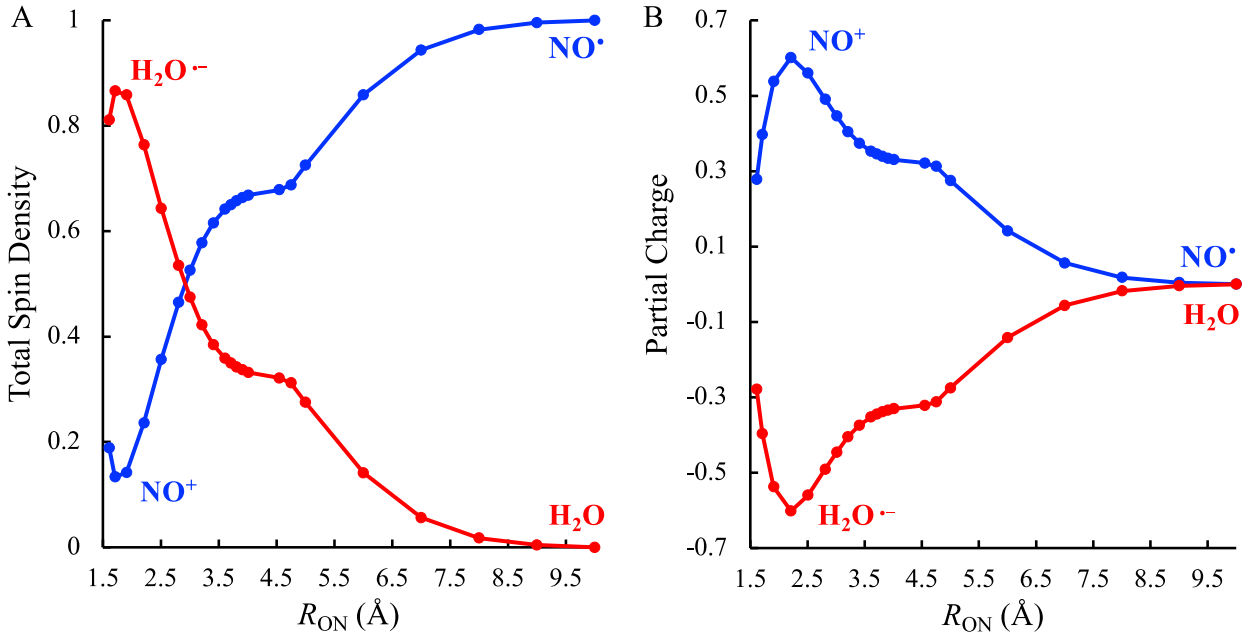

Figure 5. Löwdin population analysis for the total spin densities (panel A) and partial charges (panel B) of NO and H_2O as a function of R_{ON}. For $R_{ON} \leq 4.75$ Å, the geometries are those from Figure 4, while for $4.75 < R_{ON}$, the intermolecular distance was rigidly scanned to prevent unwanted changes to the intermolecular orientation. The total spin density and partial charge on each molecule are obtained by combining the values associated with each atom. Similar to Figure 3, this data shows evidence of electron transfer from NO ($A^2\Sigma^+$) to H_2O, creating a transient ion pair of NO^+ and H_2O^- which facilitates increased intermolecular attractions.

Figure 5A shows that, on D_2, the spin density is localized on NO at large intermolecular distances. As the molecules move closer together, the spin density becomes delocalized between both molecules. When $R_{ON} < 3.01$ Å, the spin density becomes predominately concentrated onto H_2O, which is consistent with electron transfer occurring from the electronically excited NO to the H_2O. Figure 3A shows a similar rearrangement of the spin density in the NO ($A^2\Sigma^+$) + CO system, which occurs at a slightly closer intermolecular distance between $R_{CN} = 2.75$ Å and $R_{CN} = 2.50$ Å. Turning to Figure 5B, we see the expected result of zero partial charge for both NO and H_2O at large intermolecular distances. Beginning at approximately $R_{ON} = 3.41$ Å, the partial charges dramatically increase, with the largest magnitude occurring at $R_{ON} = 2.21$ Å with values of +0.601 and -0.601 for NO and H_2O, respectively. Collectively, the data presented in both panels of Figure

5 suggests that the attractions between NO ($A^2\Sigma^+$) and H_2O are driven by electron transfer from NO to H_2O, creating a transient ion pair of NO^+ and H_2O^- which Coulombically attract one another. As such, a harpoon mechanism is operative for this system as it is for NO ($A^2\Sigma^+$) + CO.

Further support for the D_2 state exhibiting significant charge-transfer character at intermediate intermolecular distances comes from the SOMOs for the D_2 state at representative R_{ON} displayed in Figure 6. At R_{ON} = 3.61 Å, the electron density amplitude is centered on NO and shows clear 3sσ character. At the minimum energy geometry on D_2 with R_{ON} = 1.91 Å, the electron density shifts onto H_2O, consistent with electron transfer occurring from NO to H_2O. Figure 6 further shows that the SOMO at R_{ON} = 1.91 Å resembles the LUMO of H_2O, which is an antibonding σ orbital for both O-H bonds. At R_{ON} = 1.61 Å, a small amount of electron density is shifted to the 2pπ* molecular orbital state of NO, but the majority remains primarily localized on the H_2O. This redistribution of electron density from H_2O and back to NO likely reflects orbital overlap between the two molecules facilitating increased electron delocalization. Figure 5 shows that a consequence of this redistribution of electron density back onto NO is a decrease in the spin density and partial charge on H_2O at distances below R_{ON} = 1.91 Å.

Electronic State	R_{ON} (Å)			LUMO of H_2O
	1.61	1.91	3.61	
D_2 ($A^2\Sigma^+$)	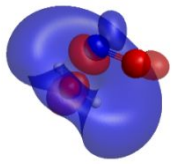	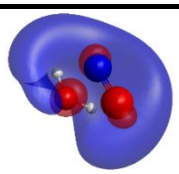	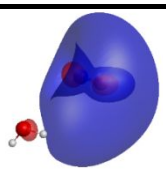	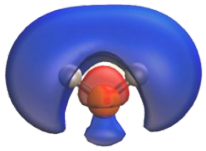

Figure 6. SOMOs for the D_2 states of NO+H_2O at representative R_{ON}; different orientations of view are used to highlight the shapes of the SOMOs better. These SOMOs were plotted using wxMacMolPlot with the following parameters: number of grid points: 150, transparency: 45, shape: solid/smooth, contour values: 0.03 for $R_{ON} \leq 1.91$ Å and 0.02 for $R_{ON} = 3.61$ Å. The LUMO of H_2O is shown to the right to aid in interpreting the SOMOs at shorter intermolecular distances. At R_{ON}=3.61 Å, the SOMO exhibits 3sσ character on NO, whereas for $R_{ON} \leq 1.91$ Å, the SOMO resembles the LUMO of H_2O. This provides further support for a harpoon mechanism.

In addition to the relative energies, we also analyzed the geometric changes in both molecules that occurred as R_{ON} was reduced along the pathway shown in Figure 4. These changes give valuable clues as to which degrees of freedom most effectively facilitate nonradiative relaxation. At both R_{ON} = 10 Å and 3.61 Å, the bond length of N-O is 1.06 Å and the O-H bond lengths are both 0.96 Å. The bond angle of H_2O slightly decreases from θ_{HOH} = 104.4° at R_{ON} = 10 Å to θ_{HOH} = 103.1° at R_{ON} = 3.61 Å. At the minimum energy geometry on D_2, R_{ON} = 1.91 Å, the N-O bond length increases to 1.09 Å but the H_2O bond angle remains at θ_{HOH} = 103.6°. The largest geometric change involves the elongation of the O-H bonds of H_2O, which increase to 1.01 Å and 0.99 Å. This elongation of the O-H bonds of H_2O is consistent with a harpoon mechanism as electron density shifts from NO into a σ^* molecular orbital of H_2O, which destabilizes the O-H bonds. At R_{ON} = 1.56 Å, the N-O bond length increases significantly to 1.14 Å, the H_2O bond angle increases to θ_{HOH} = 111.5°, and the two O-H bond lengths remain at 1.01 Å and 0.99 Å. The increase in the N-O bond length reflects the presence of electron density in the 2pπ^* MO of NO shown in Figure 6.

Because Figure 4 does not contain a low-energy D_2-D_1 conical intersection along R_{ON}, at least another nuclear degree of freedom must be involved in facilitating the nonradiative relaxation responsible for the large electronic quenching cross section of NO ($A^2\Sigma^+$)+H_2O. We first hypothesized that the O-N-O-H torsion angle (ϕ_{ONOH}) could be involved and performed a series of relaxed scans of ϕ_{ONOH} at fixed intermolecular distances. Figure 7 summarizes the variation in the energy of the D_2 state with ϕ_{ONOH} for four representative R_{ON} distances. As expected, the electronic energy depends more strongly on ϕ_{ONOH} as the intermolecular distance is reduced. Specifically, the D_2 energy ranges from -0.51 to -0.55 eV when R_{ON} = 2.01 Å and from 0.11 to -0.08 eV when R_{ON} = 1.56 Å. Figure 7 further shows that the torsion scans contain two minima and two barriers at each R_{ON}. The two minima are associated with rotational conformational isomers (rotamers), differing only in the identity of which O-H bond of water is oriented perpendicular to the NO. Both barriers are associated with C_{2v} geometries, with the larger barrier associated with NO bisecting the two O-H bonds that point towards the N-atom of NO. Overall, Figure 7 shows that distortions along ϕ_{ONOH} are associated with minimal energy increases at larger intermolecular distances, but the torsional motions become increasingly hindered as R_{ON} is reduced. In particular, the barriers at R_{ON} = 1.56 Å lie above the asymptotic limit.

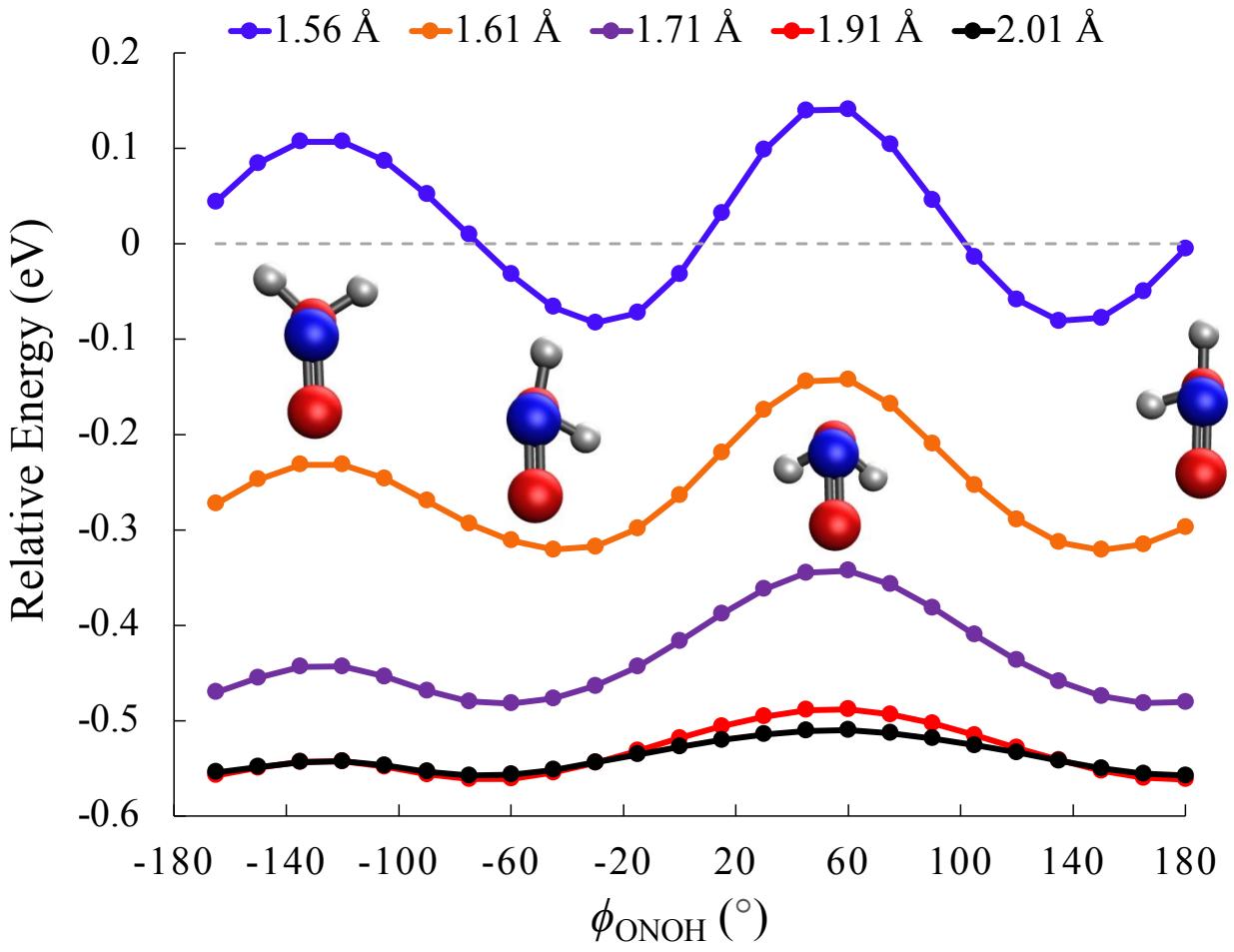

Figure 7. Cuts of the adiabatic D_2 PES for ON+H_2O as a function of the torsion angles -165° ≤ ϕ_{ONOH} ≤ 180° at R_{ON}=2.01 Å (black), R_{ON}=1.91 Å (red), R_{ON}=1.71 Å (purple), R_{ON}=1.61 Å (orange), and R_{ON}=1.56 Å (blue). All energies are reported relative to the D_2 state at R_{ON} = 10 Å. This analysis demonstrates that torsional motion on D_2 becomes increasingly hindered as R_{ON} decreases.

Figures S4-S9 in the Supporting Information show how the D_2 and D_1 energies vary with ϕ_{ONOH} at the R_{ON} values considered in Figure 7. At larger R_{ON}, varying ϕ_{ONOH} does not appreciably reduce $E_{D_2} - E_{D_1}$. For example, at R_{ON}=1.91 Å, $E_{D_2} - E_{D_1}$ ranges from 2.59 eV to 2.64 eV. The D_2-D_1 energy gap is more strongly affected by ϕ_{ONOH} at smaller R_{ON}. However, the smallest observed value of $E_{D_2} - E_{D_1}$, 0.13 eV at R_{ON}=1.56 Å and ϕ_{ONOH} = 0°, is only slightly smaller than

the minimal D_2-D_1 energy gap present in Figure 4, 0.16 eV. As such, we conclude that ϕ_{ONOH} is not relevant for the NO ($A^2\Sigma^+$) + H_2O electronic quenching pathway.

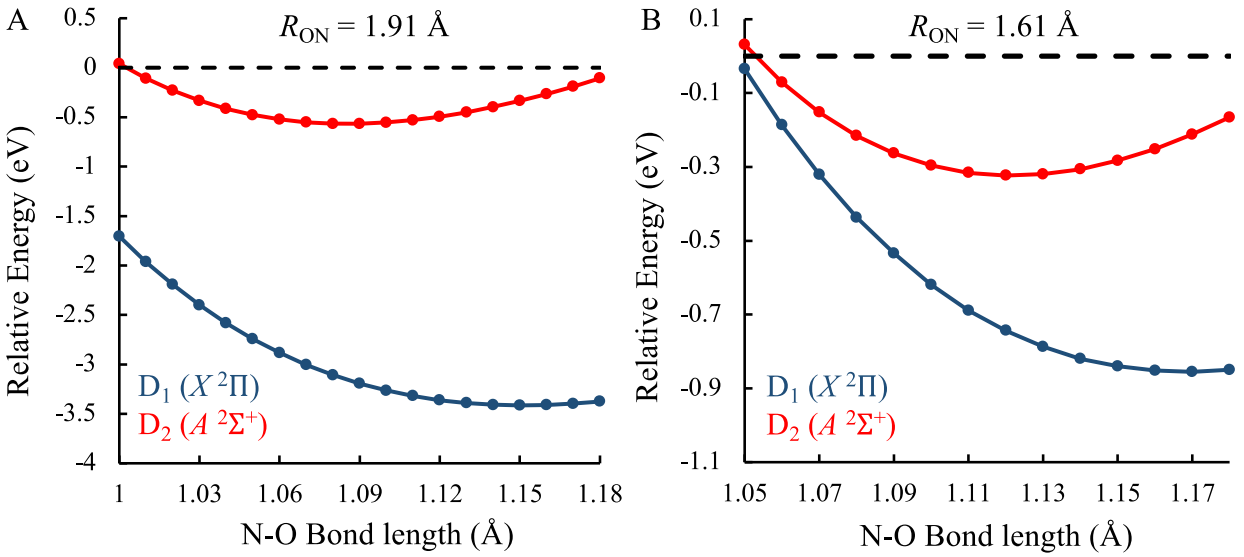

Figure 8. Cuts of the adiabatic D_1 (blue) and D_2 (red) PESs for NO+H_2O as a function of the N-O bond length for R_{ON}=1.91 Å (panel A) and R_{ON}=1.61 Å (panel B). All energies are reported relative to the D_2 state at R_{ON} = 10 Å. This analysis demonstrates that distortions of the N-O bond length do not facilitate the system reaching a D_2-D_1 conical intersection.

As mentioned above, the N-O bond length varies significantly along the path shown in Figure 4. Therefore, we explored the extent to which distortions of the N-O bond length modulate $E_{D_2} - E_{D_1}$, the analysis of which is presented in Figure 8 along with Figures S10-S11 in the Supporting Information. As shown in panel A of Figure 8, decreasing the N-O bond length somewhat reduces the D_2-D_1 energy gap when R_{ON}=1.91 Å. However, $E_{D_2} - E_{D_1}$exceeds 1.8 eV for all N-O bond lengths for which $E_{D_2} < 0$. Panel B shows that when the intermolecular distance is reduced to R_{ON}=1.61 Å, $E_{D_2} - E_{D_1}$ depends much more strongly on the N-O bond length. Indeed, decreasing the N-O bond length from 1.12 Å to 1.05 Å causes $E_{D_2} - E_{D_1}$ to decrease from 0.42 eV to 0.07 eV. Similar to Figure 4, this pathway to a D_2-D_1 conical intersection is associated with a significant increase in energy, with E_{D_2} becoming greater than the asymptotic limit. As a result, while the N-O bond length changes appreciably along the path shown in Figure 4, distorting it

away from its equilibrium value at the D_2 collision complex does not provide an effective means for the nonradiative relaxation of NO ($A^2\Sigma^+$) + H_2O.

The other geometric parameters that undergo significant changes along the path shown in Figure 4 are the O-H bond lengths of water. As such, in Figure 9, we consider how the energy of the D_2 state varies as the O-H bond lengths of water are stretched at a series of intermolecular distances. In panel A, we focus on a relaxed scan along r_{OH_A}, the O-H bond that is oriented perpendicular to NO, at four different fixed R_{ON}. Panel B presents the same data for the other O-H bond length, r_{OH_B}. To maintain a parallel orientation between NO and the stretched O-H bond, the relaxed r_{OH_B} scans shown in panel B were performed at a fixed torsion angle of ϕ_{ONOH_B} = -179.9° in addition to a fixed R_{ON}. Without this torsion angle constraint, the geometry optimization resulted in r_{OH_B} becoming oriented perpendicular to NO, thus swapping positions with r_{OH_A}.

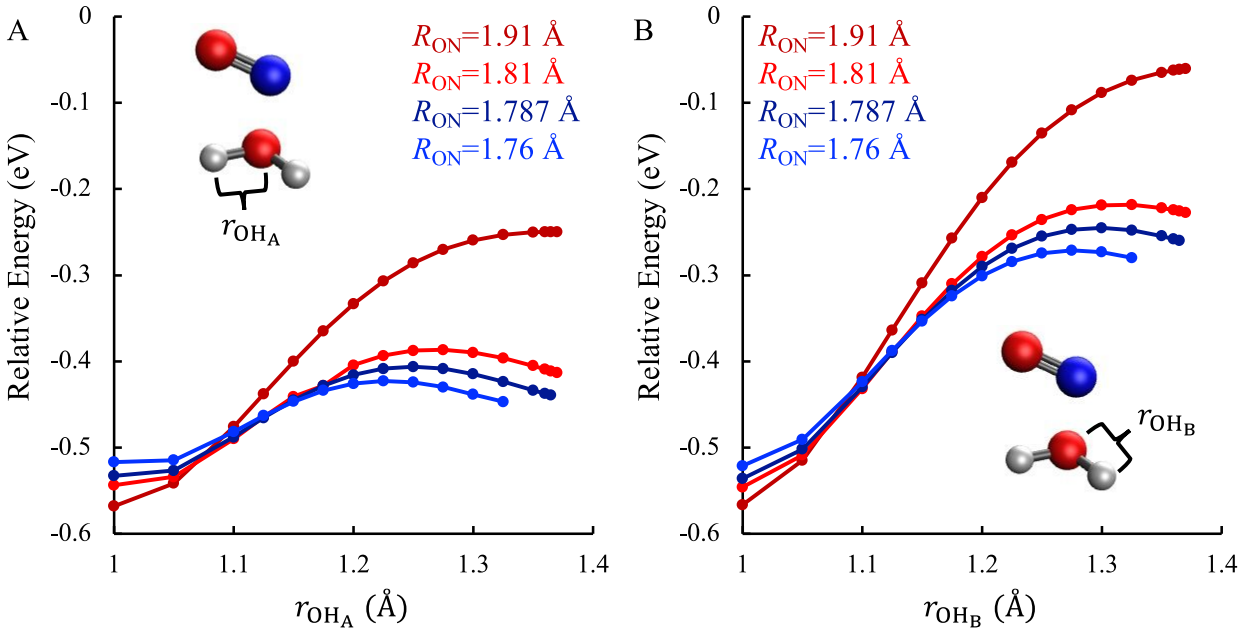

Figure 9. Cuts of the adiabatic D_2 PES of ON+H_2O as a function of the O-H bond length r_{OH_A} (panel A) or r_{OH_B} (panel B) at a fixed intermolecular distance of R_{ON} = 1.91 Å (dark red), R_{ON} = 1.81 Å (red), R_{ON} = 1.787 Å (dark blue), and R_{ON} = 1.76 Å (blue). All energies are reported relative to the D_2 state at R_{ON} = 10 Å. The O-H bond lengths r_{OH_A} and r_{OH_B} are defined in the insets. Note that increasing r_{OH_A} is associated with a modest increase in energy, ranging from 0.32 eV at R_{ON} = 1.91 Å to 0.15 eV at R_{ON} = 1.76 Å. Increasing r_{OH_B} is associated with a larger increase in E_{D_2}.

Focusing first on the E_{D_2} versus r_{OH_A} data shown in Figure 9A, stretching this O-H bond causes the energy of the D_2 state to modestly increase. The most dramatic change occurs at R_{ON}=1.91 Å, where increasing r_{OH_A} causes E_{D_2} to increase from -0.57 eV to -0.25 eV. Importantly, all of these data points lie well below the D_2 ($A^2\Sigma^+$) asymptotic limit, suggesting that these distortions are kinetically viable for the collision complex even at low temperatures. At smaller intermolecular distances, the relative energy initially increases as r_{OH_A} is stretched but eventually turns over and begins to decrease, suggesting the existence of another local minimum on the D_2 PES consistent with a significantly stretched or even broken O-H bond. The largest value of E_{D_2} observed in the relaxed scans at R_{ON} = 1.81 Å, 1.787 Å, and 1.76 Å is -0.39 eV, -0.41 eV, and

-0.42 eV, respectively. Moreover, at the elongated O-H bond lengths with r_{OH_A}>1.1 Å, decreasing R_{ON} is associated with lower energies on D_2. As such, stretching this O-H bond drives the two molecules closer together.

The data presented in panel B of Figure 9 displays similar trends as those shown in panel A. Increasing r_{OH_B}, however, has a significantly larger impact on E_{D_2} than increasing r_{OH_A}. Specifically, at R_{ON}=1.91 Å, the energy of the D_2 state ranges from -0.57 eV to -0.06 eV, which is over twice the range shown in panel A. Similarly, the barriers in the relaxed r_{OH_B} scans at R_{ON} = 1.81 Å, 1.787 Å, and 1.76 Å occur at -0.22 eV, -0.24 eV, and -0.27 eV, respectively. Because distortions along r_{OH_B} result in a 1.5-2 times greater increase in energy on D_2 than distortions along r_{OH_A}, the r_{OH_A} coordinate is likely more relevant to the photochemistry of NO ($A^2\Sigma^+$) + H_2O.

Figure 10 shows the D_2 and D_1 energies as a function of r_{OH_A} at a fixed intermolecular distance of R_{ON}=1.787 Å. The energy of the D_1 state increases rapidly as r_{OH_A} increases while E_{D_2} displays a much weaker dependence on r_{OH_A}. Indeed, the D_2 PES appears relatively flat at the scale of this plot. Importantly, the D_2-D_1 energy gap is observed to decrease as r_{OH_A} increases, reaching a minimum value of 0.06 eV at r_{OH_A} = 1.365 Å. Attempts to obtain optimized geometries at slightly larger values of r_{OH_A} were unsuccessful due to the near-degeneracy of the D_2 and D_1 states. Nevertheless, it is clear from Figure 10 that a D_2-D_1 conical intersection will occur at a geometry with R_{ON}=1.787 Å and r_{OH_A} slightly larger than 1.365 Å. Moreover, this D_2-D_1 conical intersection will form at a $E_{D_2} \approx -0.43$ eV, which lies well below the asymptotic limit and only 0.14 eV above the D_2 minimum energy geometry. As such, once the NO ($A^2\Sigma^+$) + H_2O collision complex is generated, it can readily undergo the distortions necessary to reach this D_2-D_1 conical intersection.

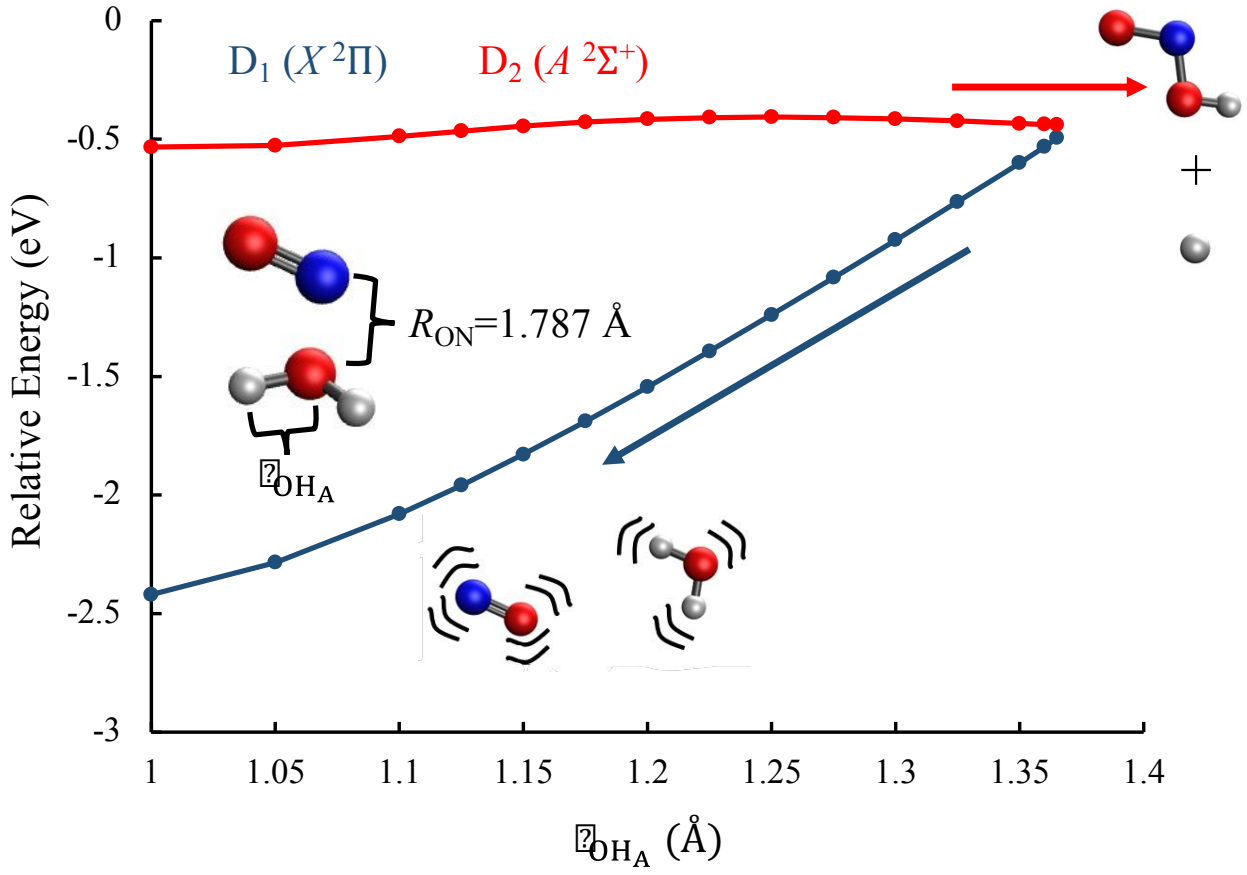

Figure 10. Cuts of the adiabatic PESs of the D_1 and D_2 states for $NO+H_2O$ as a function of r_{OH_A} at a fixed R_{ON} = 1.787 Å. All energies are reported relative to D_2 at R_{ON} = 10 Å. The inset cartoons illustrate how these PESs support both reactive electronic quenching, which produces the products HONO+H shown at the right, and nonreactive electronic quenching, which produces NO ($X^2\Pi$) and H_2O with the excess energy stored in their nuclear degrees of freedom.

Figures S12-S14 extend the analysis presented in Figure 10 to the intermolecular distances R_{ON}=1.91 Å, R_{ON}=1.81 Å, and R_{ON}=1.76 Å. For all intermolecular distances, the D_2-D_1 energy gap decreases as r_{OH_A} increases. Moreover, the initial D_2-D_1 energy gap at r_{OH_A}=1.0 Å depends sensitively on the intermolecular distance, with $E_{D_2} - E_{D_1}$ increasing as R_{ON} increases. For example, at r_{OH_A}=1.325 Å, $E_{D_2} - E_{D_1}$ is 0.09 eV when R_{ON}=1.76 Å but 1.30 eV when R_{ON}=1.91 Å. As such, this low-energy pathway to a D_2-D_1 conical intersection involves both decreasing the intermolecular distance and stretching the O-H bond that is approximately perpendicular to the

NO.

As suggested by the insets in Figure 10, the D_2-D_1 conical intersection that is accessible through a combination of decreasing R_{ON} and increasing r_{OH_A} provides a pathway for both reactive and nonreactive electronic quenching. In the case of the nonreactive electronic quenching channel (blue arrow), the dramatic stretching of the O-H bond shown in Figure 10 will likely cause the H_2O molecule to gain significant vibrational excitation in a local O-H stretching mode. Therefore, we predict that future VMI experiments on NO ($A^2\Sigma^+$)+H_2O nonreactive electronic quenching will observe a vibrational progression in the antisymmetric O-H stretching mode of H_2O with NO ($X^2\Pi$, v'', J'') products.

Turning to reactive quenching, the pathway shown in Figure 10 will result in cleavage of an O-H bond of H_2O, producing a free H-atom as previously observed in experiments by Umemoto and co-workers.[25] As discussed above, there is an energetic driving force on D_2 for decreasing R_{ON} at elongated r_{OH_A}. This supports the formation of HONO as the co-product in the reactive electronic quenching pathway. Note that the reactive pathway will involve a non-adiabatic transition from D_2 to D_1 as the D_1 state has previously been shown to adiabatically correlate to H (^2S)+HONO (X^1A').[25]

To further demonstrate the plausibility of reactive quenching, we calculated the electronic energies of *cis*-HONO+H and *trans*-HONO+H with and without zero-point energy (ZPE) corrections; this data is summarized in Table 2.[45–47] The relative energies of *cis*-HONO+H and *trans*-HONO+H were found to be -2.07 eV and -2.09 eV (-2.25 eV and -2.27 eV with ZPE corrections), respectively. These energies are both well below the asymptotic limit and hence indicate that HONO+H formation is thermodynamically favorable relative to NO ($A^2\Sigma^+$) + H_2O.

The energy released by this reaction will partition into the translational kinetic energies of the co-products along with the rotational and vibrational degrees of freedom of HONO. In particular, Umemoto and co-workers used the Doppler profiles of the H-atoms produced from the reactive electronic quenching process to determine an average translation kinetic energy of 1.17 eV.[25]

Table 2. Relative energies of predicted product outcomes from reactive electronic quenching with and without ZPE corrections.

Products	Relative Electronic Energy (eV)[a]	Relative Electronic Energy + ZPE (eV)[a,b]
cis-HONO + H (1s)	-2.07	-2.25
trans-HONO + H (1s)	-2.09	-2.27
NO (X) + OH (X) + H (1s)	0.19	-0.17

[a]Energies of possible products relative to the D_2 asymptotic limit.
[b]ZPE corrections based on experimentally determined vibrational constants.[45–47]

Analysis of the pathway shown in Figure 10 allows us to make predictions about the properties of the HONO produced in the reactive electronic quenching pathway. As suggested by the geometries shown in Figure 10, the reactive quenching pathway will preferentially form *trans*-HONO because the D_2 PES steers NO+H_2O into geometries where $|\phi_{ONOH_B}| = 180\,^\circ$. Because the ON-OH bond is formed in the reactive electronic quenching, the *trans*-HONO will likely have significant internal energy in the ON-OH stretch local mode. Similarly, because the N-O bond length of the NO moiety elongates along the reactive quenching pathway, the local vibrational stretching mode associated with this coordinate may also contain internal energy. It is unlikely that the *trans*-HONO will be generated with sufficient energy in its torsional mode to surmount the 0.515 eV barrier to *cis*-HONO. However, it is possible that this isomerization could occur through a combination of tunneling and intramolecular vibrational energy redistribution.[48] Finally, we considered the feasibility of the *trans*-HONO undergoing decomposition to generate NO and OH.

The NO+OH+H channel is marginally viable energetically, with a -0.17 eV relative energy with ZPE. However, the limited exothermicity of NO+OH+H formation and the large translational kinetic energies observed in previous experiments suggests that HONO+H will be the major product channel.

In Figures S15-S18, we analyze the D_2 and D_1 PESs as a function of r_{OH_B} at different fixed intermolecular distances. Similar to Figure 10, the D_1 state rapidly increases in energy as this O-H bond is stretched while the dependence of E_{D_2} is much more modest. As such, increasing r_{OH_B} causes the D_2-D_1 energy gap to shrink. However, this occurs at a much lower rate than what is observed in Figure 10 and Figures S12-S14. For example, when R_{ON}=1.787 Å and r_{OH_B}=1.365 Å the D_2-D_1 energy gap is 0.31 eV. In contrast, when R_{ON}=1.787 Å and r_{OH_A}=1.365 Å the D_2-D_1 energy gap is a much smaller 0.06 eV. Moreover, as shown in Figure 9 and discussed above, increasing r_{OH_B} causes a significantly greater increase in the energy of the D_2 state than increasing r_{OH_A}. As a result, the dominant electronic quenching pathway likely involves distortions along r_{OH_A} and R_{ON}, with the r_{OH_B} coordinate playing a minor role in the dynamics.

Conclusions

The PES cuts developed in this study provide clear insights into the photochemical mechanisms responsible for the reactive and nonreactive electronic quenching mechanisms of NO ($A^2\Sigma^+$) with H_2O. Long-range intermolecular attractions funnel a wide variety of initial intermolecular orientations of NO ($A^2\Sigma^+$) and H_2O to the same minimum-energy geometry at an intermolecular distance of 1.91 Å. These long-range attractive interactions were much stronger and more isotropic than those of NO ($A^2\Sigma^+$) + CO, consistent with the much greater electronic quenching cross section of NO ($A^2\Sigma^+$) + H_2O. The attractive intermolecular interactions were

shown to be driven by electron transfer from NO ($A^2\Sigma^+$) to H_2O to create a transient ion pair. This harpoon mechanism was also implicated as the source of the intermolecular attractions in the NO ($A^2\Sigma^+$) + N_2 and NO ($A^2\Sigma^+$) + CO systems. From the D_2 minimum-energy geometry, distortions involving decreasing the intermolecular distance, R_{ON}, and increasing one of the O-H bond lengths, r_{OH_A}, reduce the D_2-D_1 energy gap and ultimately lead to a D_2-D_1 conical intersection. This pathway lies well below the asymptotic limit and is associated with only a very modest energy increase relative to the minimum-energy collision complex on D_2. Moreover, this pathway accounts for both reactive and nonreactive electronic quenching.

The analysis presented in this study allows us to make clear predictions for future experimental studies on this system. The nonreactive electronic quenching pathway will tend to produce H_2O which is vibrationally excited in its antisymmetric O-H stretching mode because the pathway to the D_2-D_1 conical intersection involves a significant stretching of one of the O-H bonds. As such, future VMI studies will likely observe a vibrational progression in the antisymmetric O-H stretching mode when NO ($X^2\Sigma_g$) is formed. Reactive electronic quenching will form H atoms and *trans*-HONO with internal energy primarily localized in the ON-OH and N-O stretching modes. The branching between the nonreactive and reactive electronic quenching pathways is one major observable that we are unable to address in this study; this will be the subject of a future study employing non-adiabatic dynamics simulations.

HONO is a major source of OH radicals during the daytime.[49–52] A key radical intermediate in the atmosphere and combustion, OH radicals are arguably the most important oxidizers in these environments since they initiate the removal of gaseous pollutants.[53,54] With the lowest energy transition A^1A''–X^1A' of HONO occurring between 300 – 400 nm, this critical reservoir readily undergoes solar photolysis during the dawn and daytime hours to yield greater than 50% of the

atmospheric OH radical concentration in major cities.[55] In urban areas with large concentrations of NO_x compounds, which includes NO, in addition to atmospheric H_2O, it is likely that quenching of NO ($A^2\Sigma^+$) with H_2O at higher altitudes is a source of daytime HONO, which will readily decompose as a sink to OH + NO radicals. Therefore, this catalytic cycle of NO may serve as an important source of OH radicals, enriching the local atmospheric chemistry in polluted areas.

Conflicts of Interest

There are no conflicts of interest to declare.

Acknowledgements

This work used the Extreme Science and Engineering Discovery Environment (XSEDE), which was supported by National Science Foundation grant number ACI-1548562. This work specifically used the Comet cluster at the San Diego Supercomputer Center through allocation TG-CHE180057. Additional computational resources were provided through Center for Computational and Applied Mathematics at California State University, Fullerton. J.A.U. acknowledges funding from Project RAISE, U.S. Department of Education HSI-STEM award number P031C160152. NMK acknowledges funding support from the donors of the American Chemical Society Petroleum Research Fund (PRF# 65737-UR6) and from the Camille and Henry Dreyfus Foundation (BL-20-009).

References:

(1) Kohse-Hoinghaus, K.; Jeffries, J. B. *Applied Combustion Diagnostics*; CRC Press, 2002. https://doi.org/10.1201/9781498719414.

(2) Eckbreth, A. C. *Laser Diagnostics for Combustion Temperature and Species*; CRC Press: London, 1996. https://doi.org/10.1201/9781003077251.

(3) Finlayson-pitts, B. J.; Pitts, J. N. *Chemistry of the Upper and Lower Atmosphere*; Elsevier, 2000. https://doi.org/10.1016/B978-0-12-257060-5.X5000-X.

(4) Barker, J. R. *Progress and Problems in Atmospheric Chemistry*; Advanced Series in Physical Chemistry; WORLD SCIENTIFIC, 1995; Vol. 3. https://doi.org/10.1142/2455.

(5) Sánchez-González, R.; Eveland, W. D.; West, N. A.; Mai, C. L. N.; Bowersox, R. D. W.; North, S. W. Low-Temperature Collisional Quenching of NO $A^2\Sigma^+$ ($v' = 0$) by NO($X^2\Pi$) and O_2 between 34 and 109 K. *J. Chem. Phys.* **2014**, *141* (7), 074313. https://doi.org/10.1063/1.4892980.

(6) Drake, M. C.; Ratcliffe, J. W. High Temperature Quenching Cross Sections for Nitric Oxide Laser-Induced Fluorescence Measurements. *J. Chem. Phys.* **1993**, *98* (5), 3850–3865. https://doi.org/10.1063/1.465047.

(7) Settersten, T. B.; Patterson, B. D.; Kronemayer, H.; Sick, V.; Schulz, C.; Daily, J. W. Branching Ratios for Quenching of Nitric Oxide $A^2\Sigma^+$ ($v' = 0$) to $X^2\Pi$ ($v'' = 0$). *Phys. Chem. Chem. Phys.* **2006**, *8* (45), 5328–5338. https://doi.org/10.1039/b608619e.

(8) Paul, P. H.; Gray, J. A.; Durant, J. L.; Thoman, J. W. Collisional Electronic Quenching Rates for NO $A^2\Sigma^+$ ($v' = 0$). *Chem. Phys. Lett.* **1996**, *259* (5–6), 508–514. https://doi.org/Doi 10.1016/0009-2614(96)00763-4.

(9) Settersten, T. B.; Patterson, B. D.; Gray, J. A. Temperature- and Species-Dependent Quenching of NO $A^2\Sigma^+$ ($v' = 0$) Probed by Two-Photon Laser-Induced Fluorescence Using a Picosecond Laser. *J. Chem. Phys.* **2006**, *124* (23). https://doi.org/10.1063/1.2206783.

(10) Settersten, T. B.; Patterson, B. D.; Carter, C. D. Collisional Quenching of NO $A^2\Sigma^+$ ($v' = 0$) Between 125 and 294 K . *J. Chem. Phys.* **2009**, *130*, 204302.

(11) Kay, J. J.; Coy, S. L.; Wong, B. M.; Jungen, C.; Field, R. W. A Quantum Defect Model for the s, p, d, and f Rydberg Series of CaF. *J. Chem. Phys.* **2011**, *134* (11). https://doi.org/Artn 11431310.1063/1.3565967.

(12) Steill, J. D.; Kay, J. J.; Paterson, G.; Sharples, T. R.; Klos, J.; Costen, M. L.; Strecker, K. E.; McKendrick, K. G.; Alexander, M. H.; Chandler, D. W. Rotational Alignment of NO ($A^2\Sigma^+$) from Collisions with Ne. *J. Phys. Chem. A* **2013**, *117* (34), 8163–8174. https://doi.org/10.1021/jp402019s.

(13) Luxford, T. F. M.; Sharples, T. R.; Townsend, D.; McKendrick, K. G.; Costen, M. L. Comparative Stereodynamics in Molecule-Atom and Molecule-Molecule Rotational Energy Transfer: NO($A^2\Sigma^+$) + He and D_2. *Journal of Chemical Physics*. 2016. https://doi.org/10.1063/1.4961258.

(14) Sharples, T. R.; Luxford, T. F. M.; Townsend, D.; McKendrick, K. G.; Costen, M. L. Rotationally Inelastic Scattering of NO($A^2\Sigma^+$) + Ar: Differential Cross Sections and Rotational Angular Momentum Polarization. *J. Chem. Phys.* **2015**, *143* (20). https://doi.org/Artn 20430110.1063/1.4935962.

(15) Luxford, T. F. M.; Sharples, T. R.; McKendrick, K. G.; Costen, M. L. Experimental Testing of Ab Initio Potential Energy Surfaces: Stereodynamics of NO($A^2\Sigma^+$) + Ne Inelastic Scattering at Multiple Collision Energies. *J. Chem. Phys.* **2016**, *145* (17). https://doi.org/Artn 17430410.1063/1.4966688.

(16) Pajón-Suárez, P.; Valentín-Rodríguez, M.; Hernández-Lamoneda, R. The Interaction Potential of NO-H_2 in Ground and A Rydberg State. *Chem. Phys. Lett.* **2016**, *658*, 176–181. https://doi.org/10.1016/j.cplett.2016.06.042.

(17) Luxford, T. F. M.; Sharples, T. R.; McKendrick, K. G.; Costen, M. L. Pair-Correlated Stereodynamics for Diatom-Diatom Rotational Energy Transfer: NO($A^2\Sigma^+$) + N_2. *J. Chem. Phys.* **2017**, *147* (1). https://doi.org/10.1063/1.4979487.

(18) Parsons, B. F.; Jayson, C. J.; Szpunar, D. E.; Cook, M. M. Photodissociation of the N_2-NO Complex between 225.8 and 224.0 Nm. *J. Phys. Chem. A* **2021**, *125* (16), 3406–3414. https://doi.org/10.1021/acs.jpca.1c01920.

(19) Parsons, B. F.; Draney, A. W.; Warder, H. J.; Rivera, M. R.; Onder, M. K. Anisotropy Measurements from the Near-Threshold Photodissociation of the N_2 –NO Complex . *J. Phys. Chem. A* **2022**, *126* (8), 1386–1392. https://doi.org/10.1021/acs.jpca.1c10514.

(20) Parsons, B. F.; Rivera, M. R.; Onder, M. K. NO (*A*) Rotational State Distributions from Photodissociation of the N_2 -NO Complex. *J. Phys. Chem. A* **2022**, *126* (34), 5729–5737. https://doi.org/10.1021/acs.jpca.2c04265.

(21) Soulié, C.; Paterson, M. J. Molecular Properties and Excited State van Der Waals Potentials in the NO $A^2\Sigma^+$ + O_2 $X\Sigma_g^-$ Collision Complex. *Phys. Chem. Chem. Phys.* **2022**, *24* (13), 7983–7993. https://doi.org/10.1039/D1CP05286A.

(22) Few, J.; Fletcher, J. D.; Hancock, G.; Redmond, J. L.; Ritchie, G. A. D. An FTIR Emission Study of the Products of NO $A^2\Sigma^+$ (v = 0, 1) + O_2 Collisions. *Phys. Chem. Chem. Phys.* **2017**, *19* (18), 11289–11298. https://doi.org/10.1039/C7CP00904F.

(23) Blackshaw, K. J.; Quartey, N. K.; Korb, R. T.; Hood, D. J.; Hettwer, C. D.; Kidwell, N. M. Imaging the Nonreactive Collisional Quenching Dynamics of NO ($A^2\Sigma^+$) Radicals with O_2 ($X\Sigma_g^-$). *J. Chem. Phys.* **2019**, *151* (10), 104304. https://doi.org/10.1063/1.5109112.

(24) Soulié, C.; Paterson, M. J. Multi-State Electronic Quenching: Non-Adiabatic Pathways in NO 2 Σ + + O 2 X 3 Σ g - Scattering. *J. Chem. Phys.* **2022**, No. 2. https://doi.org/10.1063/5.0112556.

(25) Umemoto, H.; Terada, N.; Tanaka, K. Production Processes of H(D) Atoms in the Reactions of NO($A^2\Sigma^+$) With C_2H_2, C_2H_4, H_2O, and Their Isotopic Variants. *Chem. Phys.* **2000**, *259* (1), 39–47.

(26) Bloss, W. J.; Kramer, L.; Crilley, L. R.; Vu, T.; Harrison, R. M.; Shi, Z.; Lee, J. D.; Squires, F. A.; Whalley, L. K.; Slater, E.; Woodward-Massey, R.; Ye, C.; Heard, D. E.;

Tong, S.; Hou, S.; Sun, Y.; Xu, J.; Wei, L.; Fu, P. Insights into Air Pollution Chemistry and Sulphate Formation from Nitrous Acid (HONO) Measurements during Haze Events in Beijing. *Faraday Discuss.* **2021**, *226*, 223–238. https://doi.org/10.1039/d0fd00100g.

(27) Dozova, N.; Krim, L.; Alikhani, M. E.; Lacome, N. Vibrational Spectra and Structures of H_2O-NO, HDO-NO, and D_2O-NO Complexes. An IR Matrix Isolation and DFT Study. *J. Phys. Chem. A* **2006**, *110* (41), 11617–11626. https://doi.org/10.1021/jp0625614.

(28) Salmi, T.; Runeberg, N.; Halonen, L.; Lane, J. R.; Kjaergaard, H. G. Computational Vibrational and Electronic Spectroscopy of the Water Nitric Oxide Complex. *J. Phys. Chem. A* **2010**, *114* (14), 4835–4842. https://doi.org/10.1021/jp909441u.

(29) Cybulski, H.; Zuchowski, P. S.; Fernández, B.; Sadlej, J. The Water-Nitric Oxide Intermolecular Potential-Energy Surface Revisited. *J. Chem. Phys.* **2009**, *130* (10). https://doi.org/10.1063/1.3079541.

(30) Martinez Gonzalez, M.; Bravo-Rodriguez, K.; Suardiaz, R.; Garcia de la Vega, J. M.; Montero, L. A.; Sanchez-Garcia, E.; Crespo-Otero, R. Complexes of Nitric Oxide with Water and Imidazole. *Theor. Chem. Acc.* **2015**, *134* (7), 88. https://doi.org/10.1007/s00214-015-1691-x.

(31) Orenha, R. P.; San Gregorio, L. R.; Galembeck, S. E. Computational Study of the Interaction between NO, NO^+, and NO^- with H_2O. *J. Mol. Model.* **2016**, *22* (11), 276. https://doi.org/10.1007/s00894-016-3148-0.

(32) Guardado, J. L.; Hood, D. J.; Luong, K.; Kidwell, N. M.; Petit, A. S. Stereodynamic Control of Collision-Induced Nonadiabatic Dynamics of NO ($A^2\Sigma^+$) with H_2, N_2, and CO: Intermolecular Interactions Drive Collision Outcomes. *J. Phys. Chem. A* **2021**, *125* (40), 8803–8815. https://doi.org/10.1021/acs.jpca.1c05653.

(33) Li, F.; Dong, C.; Chen, J.; Liu, J.; Wang, F.; Xu, X. The Harpooning Mechanism as Evidenced in the Oxidation Reaction of the Al Atom. *Chem. Sci.* **2018**, *9* (2), 488–494. https://doi.org/10.1039/C7SC03314A.

(34) Winner, J. D.; West, N. A.; McIlvoy, M. H.; Buen, Z. D.; Bowersox, R. D. W.; North, S. W. The Role of near Resonance Electronic Energy Transfer on the Collisional Quenching of NO ($A^2\Sigma^+$) by C_6H_6 and C_6F_6 at Low Temperature. *Chemical Physics*. 2018, pp 86–92. https://doi.org/10.1016/j.chemphys.2017.12.001.

(35) Paul, P. H.; Gray, J. A.; Durant, J. L.; Thoman, J. W. Collisional Quenching Corrections for Laser-Induced Fluorescence Measurements of NO $A^2\Sigma^+$. *Am. Inst. Aeronaut. Astronaut.* **1994**, *32*, 1670–1675.

(36) Krylov, A. I. Equation-of-Motion Coupled-Cluster Methods for Open-Shell and Electronically Excited Species: The Hitchhiker's Guide to Fock Space. *Annu. Rev. Phys. Chem.* **2008**, *59*, 433–462. https://doi.org/10.1146/annurev.physchem.59.032607.093602.

(37) Krylov, A. I. The Quantum Chemistry of Open-Shell Species; 2017; Vol. 30, pp 151–224. https://doi.org/10.1002/9781119356059.ch4.

(38) Faraji, S.; Matsika, S.; Krylov, A. I. Calculations of Non-Adiabatic Couplings within Equation-of-Motion Coupled-Cluster Framework: Theory, Implementation, and

Validation against Multi-Reference Methods. *J. Chem. Phys.* **2018**, *148* (4), 044103. https://doi.org/10.1063/1.5009433.

(39) Angeli, C.; Cimiraglia, R.; Evangelisti, S.; Leininger, T.; Malrieu, J.-P. Introduction of N-Electron Valence States for Multireference Perturbation Theory. *J. Chem. Phys.* **2001**, *114* (23), 10252–10264. https://doi.org/10.1063/1.1361246.

(40) Schapiro, I.; Sivalingam, K.; Neese, F. Assessment of N-Electron Valence State Perturbation Theory for Vertical Excitation Energies. *J. Chem. Theory Comput.* **2013**, *9* (8), 3567–3580. https://doi.org/10.1021/ct400136y.

(41) Epifanovsky, E.; Gilbert, A. T. B.; Feng, X.; Lee, J.; Mao, Y.; Mardirossian, N.; Pokhilko, P.; White, A. F.; Coons, M. P.; Dempwolff, A. L.; Gan, Z.; Hait, D.; Horn, P. R.; Jacobson, L. D.; Kaliman, I.; Kussmann, J.; Lange, A. W.; Lao, K. U.; Levine, D. S.; Liu, J.; McKenzie, S. C.; Morrison, A. F.; Nanda, K. D.; Plasser, F.; Rehn, D. R.; Vidal, M. L.; You, Z.; Zhu, Y.; Alam, B.; Albrecht, B. J.; Aldossary, A.; Alguire, E.; Andersen, J. H.; Athavale, V.; Barton, D.; Begam, K.; Behn, A.; Bellonzi, N.; Bernard, Y. A.; Berquist, E. J.; Burton, H. G. A.; Carreras, A.; Carter-Fenk, K.; Chakraborty, R.; Chien, A. D.; Closser, K. D.; Cofer-Shabica, V.; Dasgupta, S.; de Wergifosse, M.; Deng, J.; Diedenhofen, M.; Do, H.; Ehlert, S.; Fang, P.-T.; Fatehi, S.; Feng, Q.; Friedhoff, T.; Gayvert, J.; Ge, Q.; Gidofalvi, G.; Goldey, M.; Gomes, J.; González-Espinoza, C. E.; Gulania, S.; Gunina, A. O.; Hanson-Heine, M. W. D.; Harbach, P. H. P.; Hauser, A.; Herbst, M. F.; Hernández Vera, M.; Hodecker, M.; Holden, Z. C.; Houck, S.; Huang, X.; Hui, K.; Huynh, B. C.; Ivanov, M.; Jász, Á.; Ji, H.; Jiang, H.; Kaduk, B.; Kähler, S.; Khistyaev, K.; Kim, J.; Kis, G.; Klunzinger, P.; Koczor-Benda, Z.; Koh, J. H.; Kosenkov, D.; Koulias, L.; Kowalczyk, T.; Krauter, C. M.; Kue, K.; Kunitsa, A.; Kus, T.; Ladjánszki, I.; Landau, A.; Lawler, K. V.; Lefrancois, D.; Lehtola, S.; Li, R. R.; Li, Y.-P.; Liang, J.; Liebenthal, M.; Lin, H.-H.; Lin, Y.-S.; Liu, F.; Liu, K.-Y.; Loipersberger, M.; Luenser, A.; Manjanath, A.; Manohar, P.; Mansoor, E.; Manzer, S. F.; Mao, S.-P.; Marenich, A. V.; Markovich, T.; Mason, S.; Maurer, S. A.; McLaughlin, P. F.; Menger, M. F. S. J.; Mewes, J.-M.; Mewes, S. A.; Morgante, P.; Mullinax, J. W.; Oosterbaan, K. J.; Paran, G.; Paul, A. C.; Paul, S. K.; Pavošević, F.; Pei, Z.; Prager, S.; Proynov, E. I.; Rák, Á.; Ramos-Cordoba, E.; Rana, B.; Rask, A. E.; Rettig, A.; Richard, R. M.; Rob, F.; Rossomme, E.; Scheele, T.; Scheurer, M.; Schneider, M.; Sergueev, N.; Sharada, S. M.; Skomorowski, W.; Small, D. W.; Stein, C. J.; Su, Y.-C.; Sundstrom, E. J.; Tao, Z.; Thirman, J.; Tornai, G. J.; Tsuchimochi, T.; Tubman, N. M.; Veccham, S. P.; Vydrov, O.; Wenzel, J.; Witte, J.; Yamada, A.; Yao, K.; Yeganeh, S.; Yost, S. R.; Zech, A.; Zhang, I. Y.; Zhang, X.; Zhang, Y.; Zuev, D.; Aspuru-Guzik, A.; Bell, A. T.; Besley, N. A.; Bravaya, K. B.; Brooks, B. R.; Casanova, D.; Chai, J.-D.; Coriani, S.; Cramer, C. J.; Cserey, G.; DePrince, A. E.; DiStasio, R. A.; Dreuw, A.; Dunietz, B. D.; Furlani, T. R.; Goddard, W. A.; Hammes-Schiffer, S.; Head-Gordon, T.; Hehre, W. J.; Hsu, C.-P.; Jagau, T.-C.; Jung, Y.; Klamt, A.; Kong, J.; Lambrecht, D. S.; Liang, W.; Mayhall, N. J.; McCurdy, C. W.; Neaton, J. B.; Ochsenfeld, C.; Parkhill, J. A.; Peverati, R.; Rassolov, V. A.; Shao, Y.; Slipchenko, L. V.; Stauch, T.; Steele, R. P.; Subotnik, J. E.; Thom, A. J. W.; Tkatchenko, A.; Truhlar, D. G.; Van Voorhis, T.; Wesolowski, T. A.; Whaley, K. B.; Woodcock, H. L.; Zimmerman, P. M.; Faraji, S.; Gill, P. M. W.; Head-Gordon, M.; Herbert, J. M.; Krylov, A. I. Software for the Frontiers of Quantum Chemistry: An Overview of Developments in the Q-Chem 5 Package. *J. Chem. Phys.* **2021**, *155* (8), 084801. https://doi.org/10.1063/5.0055522.

(42) Bode, B. M.; Gordon, M. S. MacMolPlt: A Graphical User Interface for GAMESS. *J. Mol. Graph. Model.* **1998**, *16* (3), 133–138. https://doi.org/10.1016/S1093-3263(99)00002-9.

(43) Plasser, F.; Wormit, M.; Dreuw, A. New Tools for the Systematic Analysis and Visualization of Electronic Excitations. I. Formalism. *J. Chem. Phys.* **2014**, *141* (2). https://doi.org/10.1063/1.4885819.

(44) Behn, A.; Zimmerman, P. M.; Bell, A. T.; Head-Gordon, M. Efficient Exploration of Reaction Paths via a Freezing String Method. *J. Chem. Phys.* **2011**, *135* (22), 224108. https://doi.org/10.1063/1.3664901.

(45) Huber, K.; Herzberg, G. *Constants of Diatomic Molecules*; Linstrom, P. J., Mallard, W. G., Eds.; National Institute of Standards and Technology: Gaithersburg MD, 20899. https://doi.org/https://doi.org/10.18434/T4D303.

(46) Shimanouchi, T. *Molecular Vibrational Frequencies*; Linstrom, P. J., Mallard, W. G., Eds.; National Institute of Standards and Technology: Gaithersburg MD, 20899.

(47) Jacox, M. E. *Vibrational and Electronic Energy Levels of Polyatomic Transient Molecules*; Linstrom, P. J., Mallard, W. G., Eds.; National Institute of Standards and Technology: Gaithersburg MD, 20899.

(48) Le, H. M.; Raff, L. M. Cis→trans, Trans→cis Isomerizations and N–O Bond Dissociation of Nitrous Acid (HONO) on an Ab Initio Potential Surface Obtained by Novelty Sampling and Feed-Forward Neural Network Fitting. *J. Chem. Phys.* **2008**, *128* (19), 194310. https://doi.org/10.1063/1.2918503.

(49) Perner, D.; Platt, U. Detection of Nitrous Acid in the Atmosphere by Differential Optical Absorption. *Geophys. Res. Lett.* **1979**, *6* (12), 917–920. https://doi.org/10.1029/GL006i012p00917.

(50) Spataro, F.; Ianniello, A. Sources of Atmospheric Nitrous Acid: State of the Science, Current Research Needs, and Future Prospects. *J. Air Waste Manage. Assoc.* **2014**, *64* (11), 1232–1250. https://doi.org/10.1080/10962247.2014.952846.

(51) VandenBoer, T. C.; Young, C. J.; Talukdar, R. K.; Markovic, M. Z.; Brown, S. S.; Roberts, J. M.; Murphy, J. G. Nocturnal Loss and Daytime Source of Nitrous Acid through Reactive Uptake and Displacement. *Nat. Geosci.* **2015**, *8* (1), 55–60. https://doi.org/10.1038/ngeo2298.

(52) Lammel, G.; Cape, J. N. Nitrous Acid and Nitrite in the Atmosphere. *Chem. Soc. Rev.* **1996**, *25* (5), 361. https://doi.org/10.1039/cs9962500361.

(53) Emmerson, K. M.; Carslaw, N. Night-Time Radical Chemistry during the TORCH Campaign. *Atmos. Environ.* **2009**, *43* (20), 3220–3226. https://doi.org/10.1016/j.atmosenv.2009.03.042.

(54) Stone, D.; Whalley, L. K.; Heard, D. E. Tropospheric OH and HO_2 Radicals: Field Measurements and Model Comparisons. *Chem. Soc. Rev.* **2012**, *41* (19), 6348. https://doi.org/10.1039/c2cs35140d.

(55) Ren, X.; Harder, H.; Martinez, M.; Lesher, R. L.; Oliger, A.; Simpas, J. B.; Brune, W. H.; Schwab, J. J.; Demerjian, K. L.; He, Y.; Zhou, X.; Gao, H. OH and HO_2 Chemistry in the Urban Atmosphere of New York City. *Atmos. Environ.* **2003**, *37* (26), 3639–3651. https://doi.org/10.1016/S1352-2310(03)00459-X.